Monsoon-Enhanced Silicate Weathering as a New Atmospheric CO 2 Consumption Mechanism Contributing to Fast Late Miocene Global Cooling

Yibo Yang, Chengcheng Ye, Albert Galy, Xiaomin Fang, Yong Xue, Yudong Liu, Rongsheng Yang, Ran Zhang, Wenxia Han, Weilin Zhang, et al.

Paleoceanography and Paleoclimatology

RESEARCH ARTICLE
10.1029/2020PA004008

Key Points:

- Late Cenozoic clay mineral records of silicate weathering intensity in the northeastern Tibetan Plateau and Chinese Loess Plateau
- Silicate weathering intensity has been greatly enhanced over the East Asian monsoon region at ~9–7 Ma
- Monsoon-forced silicate weathering acting as an emerging CO_2 sink may regulate fast global cooling since ~7 Ma

Supporting Information:

- Supporting Information S1

Correspondence to:
Y. Yang and X. Fang,
yangyibo@itpcas.ac.cn; fangxm@itpcas.ac.cn

Citation:
Yang, Y., Ye, C., Galy, A., Fang, X., Xue, Y., Liu, Y., et al. (2021). Monsoon-enhanced silicate weathering as a new atmospheric CO_2 consumption mechanism contributing to fast late Miocene global cooling. *Paleoceanography and Paleoclimatology*, *36*, e2020PA004008. https://doi.org/10.1029/2020PA004008

Received 16 JUN 2020
Accepted 11 DEC 2020

Monsoon-Enhanced Silicate Weathering as a New Atmospheric CO_2 Consumption Mechanism Contributing to Fast Late Miocene Global Cooling

Yibo Yang[1,2], Chengcheng Ye[2], Albert Galy[3], Xiaomin Fang[1,2,4], Yong Xue[5], Yudong Liu[2,4], Rongsheng Yang[2,4], Ran Zhang[6], Wenxia Han[7], Weilin Zhang[1,2], and Xiaobai Ruan[2,3]

[1]CAS Center for Excellence in Tibetan Plateau Earth Sciences, Chinese Academy of Sciences, Beijing, China, [2]Key Laboratory of Continental Collision and Plateau Uplift, Institute of Tibetan Plateau Research, Chinese Academy of Sciences, Beijing, China, [3]Centre de Recherches Pétrographiques et Géochimiques, UMR7358, CNRS, Université de Lorraine, Nancy, France, [4]University of Chinese Academy of Sciences, Beijing, China, [5]Micro Structure Analytical Laboratory, Peking University, Beijing, China, [6]Climate Change Research Center, Institute of Atmospheric Physics, Chinese Academy of Sciences, Beijing, China, [7]Shandong Provincial Key Laboratory of Water and Soil Conservation and Environmental Protection, College of Resources and Environment Sciences, Linyi University, Linyi, China

Abstract Fast late Miocene global cooling since ~7 Ma accompanied by less changeable atmospheric CO_2 levels revealed by existing proxy reconstructions has suggested an intriguing tectonic-climate link that remains controversial. Here, we present late Cenozoic clay mineral records of the silicate weathering intensity from the Chinese Loess Plateau and northeastern Tibetan Plateau to demonstrate a remarkable increase in silicate weathering intensity at ~9–7 Ma induced by enhanced monsoon. This change caused CO_2 consumption ranging from 0.18 to 1.8 × 10^{11} mol C yr^{-1} over the East Asian monsoon region, accounting for 0.2%–2% of the modern continental silicate weathering flux, thus providing an additional atmospheric CO_2 sink. Moreover, we propose that this additional sink may have contributed to the large atmospheric CO_2 consumption and fast global cooling in the late Miocene, which ultimately caused the onset of the Northern Hemisphere glaciation at ~7 Ma.

1. Introduction

The interactions between tectonics and climate related to the Tibetan Plateau (TP) uplift, Asian monsoon circulation, Cenozoic global cooling, and atmospheric CO_2 consumption are intriguing issues that have been discussed since the late 1980s (Raymo, 1988), but the tightness of these links and the magnitudes of their importance have been widely debated over 3 decades (e.g., Caves Rugenstein et al., 2019; Clift et al., 2008; France-Lanord & Derry, 1997; Lenard et al., 2020; Macdonald et al., 2019; Park et al., 2020; Raymo & Ruddiman, 1992). In particular, a new compilation of globally distributed sea surface temperature records reveals that fast late Miocene cooling occurred synchronously in both hemispheres at ~7–5.4 Ma and that this period of rapid cooling was superimposed on the late Miocene long-term gentle cooling trend (Hebert et al., 2016). If a tight temperature-CO_2 link did exist, as seen in an Eocene greenhouse world (Anagnostou et al., 2016, 2020), a hypothesized decline in atmospheric CO_2 levels between ~8 and 6 Ma seems likely to have occurred (Bolton & Stoll, 2013; Cerling et al., 1997). However, this decline is not only largely missing from the late Miocene existing atmospheric CO_2 reconstructions (Beerling & Royer, 2011) but also inconsistent with the relatively stable CO_2 input from volcanic degassing, as suggested by the invariable sea floor spreading rate (Muller et al., 2008). Therefore, the fact that atmospheric CO_2 reconstructions do not show a similar drop in global temperatures means that either the CO_2 reconstructions are yet to be accurate and high enough resolution to resolve such a drop, which requires an additional atmospheric CO_2 consumption process prior to ~7 Ma accounting for this drop, or other feedbacks such as a very low Earth climate sensitivity in a late Miocene cooling world (e.g., Farnsworth et al., 2019; Hansen et al., 2013; Rohling et al., 2012) may be in play. Until now, the driving force of this late Miocene rapid cooling at ~7–5.4 Ma remains unclear.

The late Miocene evolution of the East Asian monsoon climate was assumed to be primarily driven by global cooling, Antarctic glaciation, and the tectonic uplift of the TP (e.g., An et al., 2001; Ao et al., 2016;

Clift et al., 2014; Miao et al., 2011; Tada et al., 2016; Zoura et al., 2019). Thus, the East Asian monsoon region provides an ideal case for revealing intriguing and complex tectonic-climate interactions. For example, many previous studies have investigated Asian monsoon development with changes in Neogene mountain exhumation, silicate weathering, and the associated CO_2 consumption (e.g., Clift et al., 2008, 2014; Lu et al., 2020; Van Hoang et al., 2010; Wan et al., 2012). In particular, the Chinese Loess Plateau (CLP) in north China, an area that is very sensitive to variations in the East Asian summer and winter monsoons, has accumulated long, continuous eolian sequences within the large platforms on the eastern portion of the plateau (An et al., 2001). These eolian sequences consist of upper Quaternary loess-paleosol deposits and lower Red Clay sequence that are composed of less-altered materials transported from arid areas in the northern TP and inland Asia (e.g., Z. Chen & Li, 2013; Nie et al., 2014; Y. Sun et al., 2008). Generally, the less-altered eolian material was further weathered in the CLP region, which led to a significant loss of base cations. Thus, these eolian sequences are useful archives for reconstructing the evolution of the East Asian monsoon (e.g., An et al., 2001; Y. Sun et al, 2015). The onset of eolian Red Clay accumulation on the CLP at ~8 Ma (Qiang et al., 2001; Song et al., 2001) may support an enhancement of the East Asian monsoon circulations since then. However, a quantitative estimate of the magnitude of monsoon climate-regulating CO_2 consumption by enhanced silicate weathering and its potential global impact at ~8 Ma has never been investigated, which is mainly due to the lack of long-term reliable silicate weathering records from which to reconstruct the changes in the magnitude of the silicate weathering intensity (SWI) and to quantitatively estimate the flux of the "additional" CO_2 sink over East Asia.

The East Asian summer monsoon (EASM) provides a majority of the moisture for the entire CLP and the eastern portion of the northeastern TP (e.g., F. Chen et al., 2008; Z. Li et al., 2015; Zan et al., 2015), while the East Asian winter monsoon and the westerlies transport dust from the arid Asian inland to the downwind northeastern TP and CLP regions since at least ~9–7 Ma (An et al., 2001; M. Fan et al., 2006; Nie et al., 2014; Y. Yang et al., 2017). Furthermore, the 9–7 Ma mountain building in the northeastern TP (e.g., Lease et al., 2007; J. Li et al., 2014; Saylor et al., 2018; Yang et al., 2019; D. W. Zheng et al., 2006) also exposed a large amount of fresh upper crustal rocks that were transported to adjacent drainage basins by rivers and to the downwind CLP region by wind. Provenance studies also suggest that the northeastern TP acts as a dominant source area for Neogene fluvial-lake sediments in adjacent fluvial basins (e.g., Fang et al., 2016; S. Liu et al., 2019; Yang et al., 2019) and eolian deposits on the CLP (e.g., Bird et al., 2020; Z. Chen & Li, 2013). Silicate minerals in these fluvial and eolian sequences can be weathered, which involves the removal of base cations (e.g., Ca, Na, K, and Mg) and the concomitant formation of clay minerals (Nesbitt & Young, 1982). The degree of alternation of silicate minerals (i.e., the SWI) is controlled by the silicate mineral supply (physical erosion rate) and climatic parameters (pCO_2, temperature, rainfall, etc.) (e.g., Rasmussen et al., 2011). The accumulation and preservation of these weathering products in fluvio-lacustrine and eolian sequences could, in turn, be used to investigate the erosion and weathering processes related to regional tectonic uplift and climate change. Therefore, evaluating the degradation of silicate minerals and the assemblages of newly formed clay minerals is a useful tool for revealing the late Cenozoic East Asian monsoon evolution and the associated carbon consumption processes. In this study, we present two records of the late Cenozoic regional SWI based on clay mineral assemblages in the East Asian monsoon region, with one retrieved from a fluvial sequence (12.2–5.1 Ma) in the Linxia Basin on the northeastern TP (also within the area of the western CLP) and the other from a typical eolian Red Clay-loess/paleosol sequence (6.2–0 Ma) in the eastern CLP (Figure 1). This suite of clay records can eliminate much of the uncertainty from different proxies across a broad region (e.g., Fang et al., 2019). By using these records, we attempt to obtain a first-order estimate of the changes in the SWI and the silicate weathering flux over East Asia and assess the potential role of silicate weathering in regulating the global climate as a geological CO_2 sink.

2. Setting and Stratigraphy

The Linxia Basin, situated on the northeastern TP, is a sub-basin of the larger Paleocene-Miocene basin complex known as the Longzhong Basin (Figure S1). Several eastward-trending ranges of the NW-trending Qilian Shan Mountains stretch into and extend below the Longzhong Basin, thus separating the western part of the Longzhong Basin into several sub-basins, such as the Xining, Lanzhou, and Linxia basins (Figure 1b). The Linxia Basin has elevations of approximately 1,800–2,600 m above sea level (asl), with the

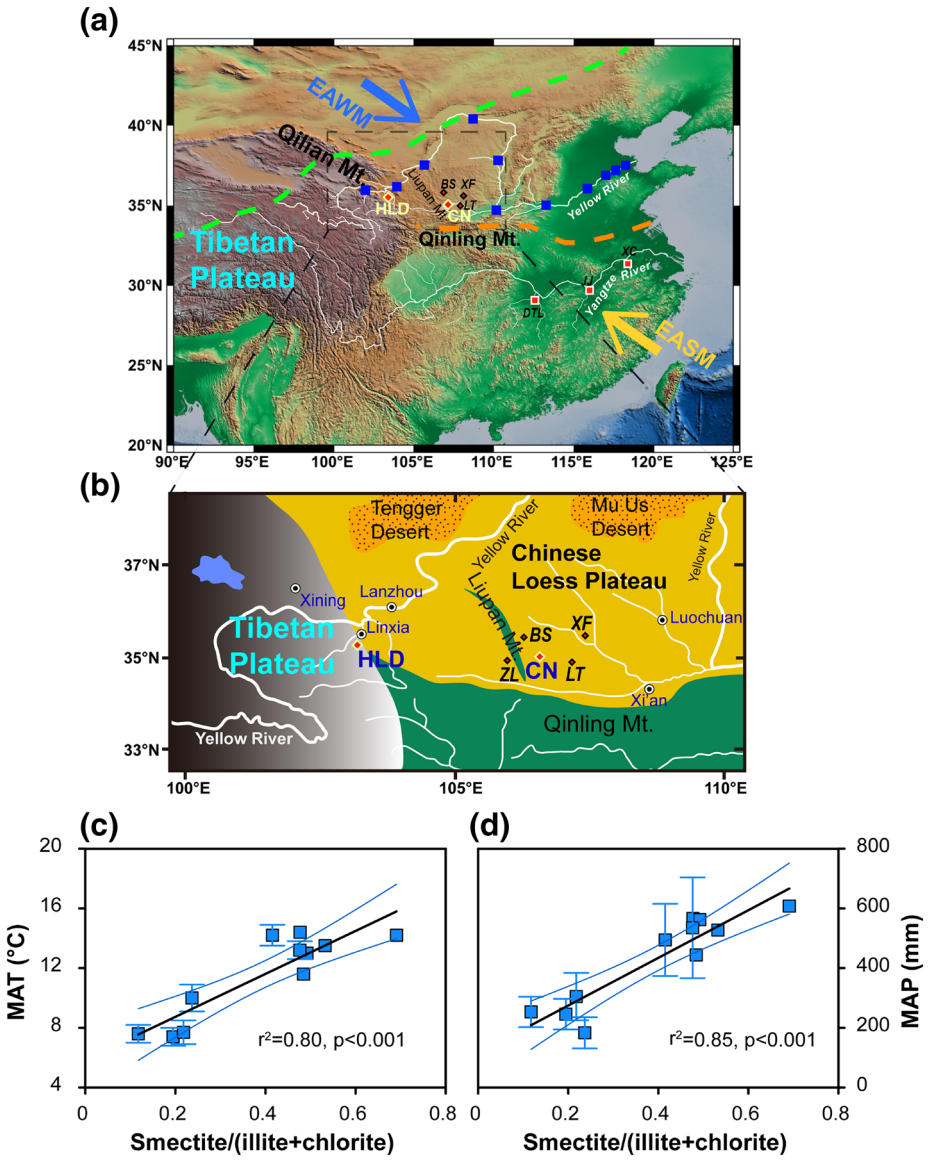

Figure 1. The study locations and regional settings. (a) Locations of the Heilinding (HLD) section in the Linxia Basin and the Chaona (CN) section in the eastern Chinese Loess Plateau (CLP) to the east of Liupan Mountain (Mt.). Three locations of red soil (red squares; Dongting Lake region [DTL]; Jiujiang [JJ]; Xuancheng [XC]) are marked. Bold arrows show the East Asian summer monsoon (EASM) and winter monsoon (EAWM). The modern Asian summer monsoon limit is shown by a green dashed line (Chen et al., 2008). The southern and northern climatic boundary of the East Asian monsoon region is marked by the Qinling Mountains (Mts.)-Huai River Line, as shown by an orange dashed line. (b) Location map showing the study sites with respect to the northeastern Tibetan Plateau (TP) and the CLP. The locations of eolian sections (red diamonds; Baishui [BS]; Lingtai [LT]; Xifeng [XF]; Zhuanglang [ZL]) are also marked. (c)-(d) Correlations between the smectite/(illite + chlorite) ratio and mean annual temperature (MAT) and mean annual precipitation (MAP) (1981–2010) for modern Yellow River fluvial sediments (blue squares in Figure 1a). Clay mineral ratios are calculated from Zhao et al. (2018), and meteorological data (with one σ error when applicable) are from nearby meteorological stations from the China Meteorological Data Service Center. Black and blue lines are linear fits of meteorological data and the 95% confidence limits, respectively.

surrounding mountains at elevations of approximately 3,000–4,000 m asl. The basin is bounded by the Maxian Shan Mountains to the north, the Laji Shan and Jishi Shan Mountains to the west and the West Qin Ling Mountains to the south and open to the western CLP to the east (Figure S1; Fang et al., 2016). Cenozoic sediments with thicknesses up to 1,600 m fill the basin, and they consist mainly of red beds of

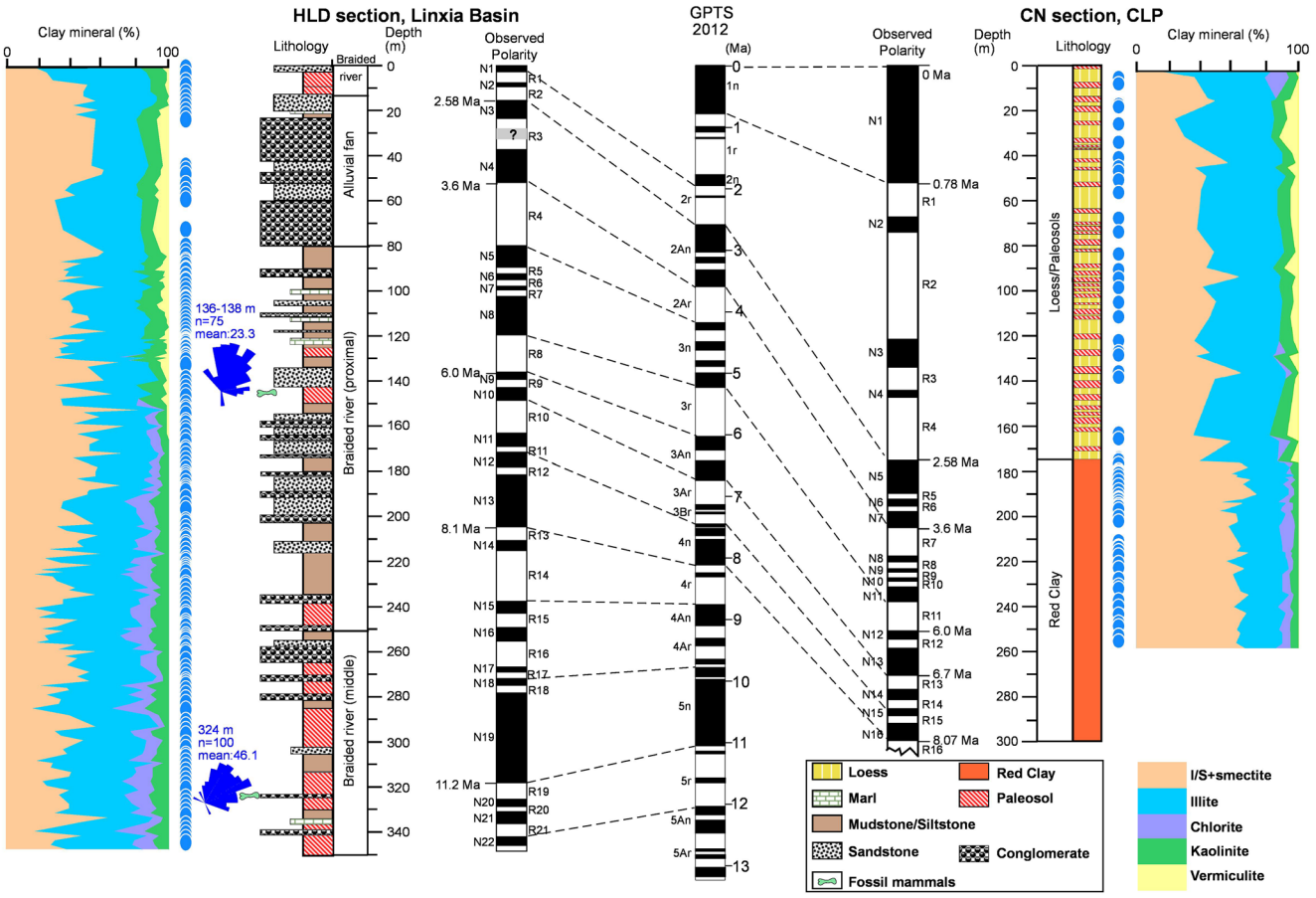

Figure 2. Lithology, magnetostratigraphy and clay mineral distributions in the HLD and CN sections. Dashed lines show the correlations of the observed magnetic polarities (HLD section, Fang et al., 2016; CN section, Song et al., 2001) with the Geomagnetic Polarity Time Scale (GPTS; Ogg, 2012). Blue dots mark the locations of the samples along the sections. Paleocurrent directions are plotted on rose diagrams. n refers to the number of measurements. Note that the paleocurrent direction plotted around the conglomerate layer at ~324 m (where fossil mammal *Platybelodon* is found) at the HLD section is measured from the corresponding *Platybelodon*-bearing conglomerate layer at the nearby LG section (Figure S1; Zhang et al. 2019). I/S denotes the illite/smectite mixed layer. CN, Chaona; HLD, Heilinding.

fluvio-lacustrine mudstones and siltstones in the center and thick strata of gray to reddish-brown conglomerates and sandstones on the margins. The Linxia Basin is between the northeast TP and the western CLP. The Liupan Shan, situated at the center of the CLP, consists of a series of NNW-ESE-oriented ranges that separate the CLP into western and eastern parts.

The 824.7-m-thick fluvial Heilinding (HLD) composite section (35°22.5′N, 103°19.1′E, 2,406 m asl) in the southern margin of the Linxia Basin includes an HLD outcrop, the top HZT drilling core, and the bottom HZ drilling core. The magnetostratigraphy of the HLD section was well constrained by two kinds of mammal fossils, a lower *Platybelodon* fauna and an upper *Hipparion* fauna, which have been found in a conglomerate bed at a depth of 322 m and in a sandstone bed at a depth of 143 m below the surface, respectively (Figure 2; Fang et al., 2016). This study focused on the upper 347 m-thick sediments (HLD outcrop and HZT drilling core) ranging between 12.2 and 1.8 Ma. The depth-to-age correlation was performed by linear interpolation using average sediment accumulation rates between the main magnetic polarity boundaries. The chosen interval is characterized by mudstones and siltstones interbedded with some layers of sandstones and conglomerate lenses and exhibits upward coarsening (Figure 2). Notably, the section contains abundant layers of paleosols between 347 m and 236 m and fewer paleosols above 236 m.

The eolian Chaona (CN) section (35°12′N, 107°7′E, 1,463 m asl) consists of a 175-m-thick upper part containing a loess-paleosol sequence and a 125-m-thick lower part containing a Red Clay sequence characterized

by reddish soils and calcareous nodules (Figure 2). Detailed magnetostratigraphy has constrained the formation of the loess-paleosol sequence between 2.6 and 0 Ma and that of the Red Clay sequence between 8.1 and 2.6 Ma (Song et al., 2001). The lower unit of the Red Clay (6.2 to ~8 Ma) on the eastern CLP is assumed to be a water-reworked deposit that was transported over a short distance from formerly deposited (probably eolian) clastic sediments and weathering materials by alluvial and slope processes, as suggested by morphological, grain size and geochemical properties (Guo et al., 2001). This water-reworking process is probably linked to fault activity in the Liupan Mountains since ~8 Ma (D. W. Zheng et al., 2006). However, the post-6.2 Ma Red Clay sequences are typical *in situ* eolian deposits, as shown by similar macromorphological features and identical variations in magnetic susceptibility across the eastern CLP region (Guo et al., 2001). Here, we only study the portion higher than 259 m (<~6.2 Ma). The modern climate of the two study sections was determined from nearby meteorological stations. The MAP and MAT of Hezhen City, which is ~7 km northeast of the HLD section in the Linxia Basin, are 5.8°C and 592.7 mm, respectively, and they reasonably reflect the average climatic conditions of this section. The MAT and MAP of Lingtai City, which is ~37 km east of the CN section, are values of 9.4°C and 586.4 mm, respectively, and they are used to represent the conditions of this section. The precipitation between June and September associated with the EASM accounts for ~60%–70% of the precipitation in all of the above sections (Figure S2).

3. Materials and Methods

A total of 165 samples from the HLD section (with an ~60 kyr resolution on average), two local late Quaternary eolian loess samples from the Linxia Basin, and 63 samples from the CN section (with an ~100 kyr resolution on average) were chosen for the clay mineral analysis. The clay fraction (<2 μm) was separated from the bulk samples according to Stokes' Law after the removal of organics by diluted H_2O_2 in a water bath at 50°C for over 8 h until the solution nearly dried out. Then, 10% (v/v) acetic acid was added to remove carbonate in a water bath at 50°C for at least 6 h. The residual acetic acid and free ions were washed with deionized water to help the deflocculation of clays with the occasional addition of 1–2 ml $NH_3{\cdot}H_2O$. The clay sample was prepared using pipetting before the X-ray diffraction (XRD) analysis. The air-dried (AD), ethylene glycol-saturated (EG), and heated XRD patterns for each sample were used in clay mineral identification and semiquantitative calculations (see details in Yang et al., 2019). In brief, each sample was suspended and deposited onto glass slides and allowed to air-dry at room temperature. After performing the XRD analysis on the AD samples, they were treated with ethylene glycol vapor for 24 h and heated at 450°C for 2 h after ethylene glycol solvation. Then, each sample included the AD, EG, and heated XRD patterns. To assess the bulk mineralogy of the CN section, six samples (four loess-paleosol samples and two Red Clay samples) were chosen to determine major mineral types using XRD analysis. The XRD patterns were measured using a Rigaku D/MAX-2000 diffractometer (Cu, Kα, 1.5406 Å, 40 kV, 100 mA, step 0.02°, 10°/min) at the Micro Structure Analytical Laboratory, Peking University.

Clay mineral identification and semiquantitative estimates were performed with Jade 6.5 software by using diagnostic peak parameters (e.g., position, height, and area) of the 00l basal reflections for each clay mineral (Moore & Reynolds, 1997). The distinction between kaolinite and chlorite is based on the (002) peak (3.58 Å) of kaolinite and the (004) peak (3.54 Å) of chlorite. The smectite proportion in mixed-layered illite/smectite (I/S) was estimated following the method described in Reynolds (1980). K-saturation and progressive heating treatments were further employed to identify vermiculite minerals from chlorite (Barnhisel & Bertsch, 1989). Specifically, the ~1.42 nm decrease in peak intensity and 1.0 nm increase in peak intensity after K^+ saturation and the collapse of the 1.41 nm peak in the K-air diffractogram toward 1.0 nm during progressive heating collectively identify the presence of vermiculite minerals. For bulk samples, quartz, plagioclase, K-feldspar, and calcite were identified using 4.26 Å (100), 3.18 Å (040), 3.23 Å (002), and 3.03 Å (104), respectively. Relative contents of each mineral are calculated by using K-value method with a reference material of corundum (Moore & Reynolds, 1997).

To assess the correlation between the element and clay mineral assemblage in the CN section and the elemental comparability between the CN section and Baishui (BS) section with previously reported elemental composition (S. Xiong et al., 2010), we also measured the major elements of 43 bulk samples in the CN section after the removal of carbonate with 10% (v/v) acetic acid at room temperature for at least 12 h

with occasional oscillation. The acid residual samples were digested by pressurized acid digestion using a mixture of HNO_3/HF in a Teflon digestion vessel (Y. Yang et al., 2015). The digestant was diluted to ~50 ml for analysis using ultrapure water. The major elements were determined by ICP-OES (Leeman Labs Prodigy-H) at the Institute of TP Research, Chinese Academy of Sciences. Standard samples (GSR-1 and GSR-2) and blank samples were used for quality control. Replicate analyses of samples show the relative standard deviations for all elements <2%.

4. Results

The major minerals in bulk samples of the CN section are quartz, plagioclase, K-feldspar, clay + mica with varying contents of calcite (Figure S3), which is similar to those for the HLD section (Y. Yang et al., 2016). The clay minerals in the HLD and CN sections show similar compositions with high proportions of I/S and illite, less chlorite and kaolinite, and a limited amount of smectite and vermiculite (Figures 2 and S4). Here, we group I/S and smectite as "total smectite" because I/S is often considered the diagenetic transformation product of smectite illitization in old sequences (Chamley, 1989). Total smectite and illite are the dominant clay minerals and collectively account for 87% in the HLD section, 88% in the CN section, and ~80% in local loess in the Linxia Basin on average. In addition, a small amount of vermiculite minerals (generally <10%) appear in the post-3 Ma eolian sediments in the CN section and the post-7.2 Ma HLD section sediments (Figure 2).

Generally, the (I/S + smectite)/(illite + chlorite) ratio in the HLD section exhibits a relatively stable trend before 8–9 Ma and a significant rise since ~8 Ma, followed by a relatively high value at 6–2.6 Ma and a monotonic decrease since 2.6 Ma, eventually approaching the modern loess composition (Figure 3). The ratio in the CN section shows a consistent evolution and value range with those of the HLD section since 6.2 Ma. More specifically, a temporal peak between 3.4 Ma and 2.6 Ma and a persistent decrease since 2.6 Ma are obvious in the two sections (Figure 3). The Na_2O_3/Al_2O_3 ratio in the CN section ranging from 0.04 to 0.13 shows a consistent evolution with the (I/S + smectite)/(illite + chlorite) ratio since 6.2 Ma (Figure 3).

5. Discussion

5.1. Validity of Clay Minerals as SWI Proxies

Chlorite and illite reflect weak silicate weathering in cold and/or arid environments, whereas smectite, vermiculite, I/S, and kaolinite indicate strong silicate weathering under humid temperate climates (Chamley, 1989), which is consistent with the clay mineral distribution in China (Y. Xiong & Li, 1990). In both study sections, the kaolinite contents are generally <10%, with an average of 5%–6% (Figure 2), suggesting that kaolinite cannot be used as a convincing indicator of a strong SWI. The most widespread clay diagenesis in sedimentary basins is the illitization of smectite, which always yields lower smectite proportions and higher illite proportions in I/S with increasing burial depth (e.g., Chamley, 1989). The lack of a downward increase in the illite content (Figure 2) and a downward decrease in the smectite proportion in I/S (Figure S5) in both sections suggests limited diagenetic effects. Because smectite, I/S and illite account for >80% of the clays in both sections, the (I/S + smectite)/(illite + chlorite) ratio is the best candidate for tracing changes in the SWI. The smectite/(illite + chlorite) ratios of the modern fluvial sediments in the Yellow River drainage basin (Zhao et al., 2018), which drains North China and spans distinct climatic and lithological regimes, also exhibit first-order climatic control (Figures 1c and 1d; Table S1). This may suggest that the impact of provenance changes on the clay mineral assemblage was low because the long Yellow River drains different lithological units across a broad swath of China (see major distributed strata in S. Xiong et al., 2010). In this regard, the variation in the (I/S + smectite)/(illite + chlorite) ratio (here, the term "I/S + smectite" indicates the total smectite content before diagenetic alteration during burial) in the two sections reflects long-term changes in the SWI at a regional scale, which is also proven to be a useful proxy of the SWI and paleoenvironment in the northeastern TP during the early Cenozoic (Fang et al., 2019) and even in NE China during the Late Cretaceous (Y. Gao et al. 2015).

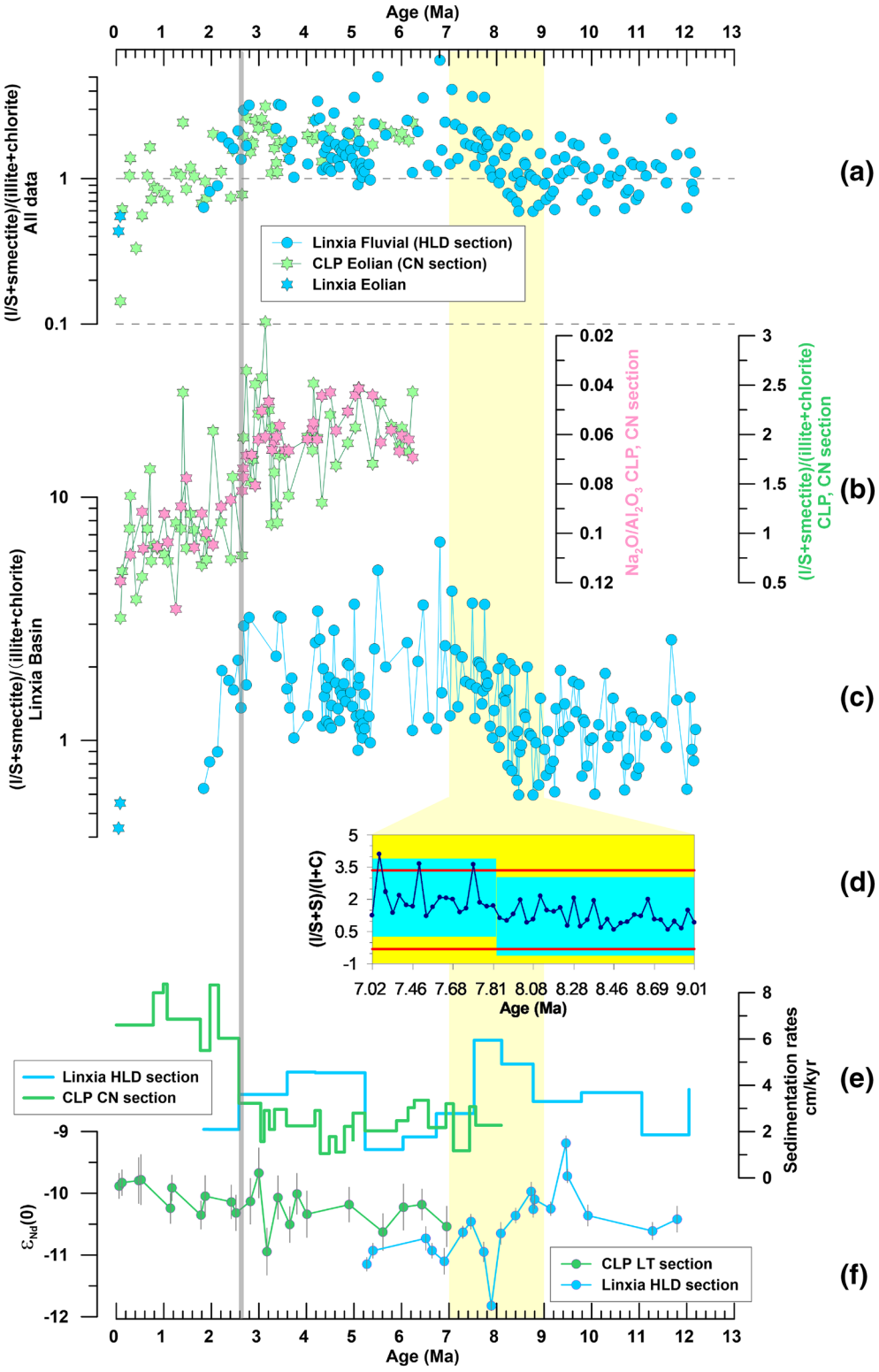
Age (Ma)
(I/S+smectite)/(illite+chlorite) All data
Linxia Fluvial (HLD section)
CLP Eolian (CN section)
Linxia Eolian
(a)
Na_2O/Al_2O_3 CLP, CN section
(I/S+smectite)/(illite+chlorite) CLP, CN section
(b)
(I/S+smectite)/(illite+chlorite) Linxia Basin
(c)
(I/S+S)/(I+C)
(d)
Linxia HLD section
CLP CN section
Sedimentation rates cm/kyr
(e)
$\varepsilon_{Nd}(0)$
CLP LT section
Linxia HLD section
(f)

Figure 3.

Generally, the SWI in source area weathering is mainly controlled by physical erosion and climatic conditions. The former determines the duration of time that fresh rock is exposed within the weathering profile, and the latter controls the weathering reaction dynamics. Thus, intense physical erosion in tectonically active regions is expected to reduce the silicate weathering duration time in source areas under relatively stable climatic conditions. Moreover, when weathering products and fresh rock fragments are transported to the deposition area (e.g., floodplains), they may be subject to weathering again. This so-called secondary weathering is quite common and significant in a large drainage basin with a long transfer time through the floodplain, e.g., in the Ganga basin (Lupker et al., 2012). Floodplain weathering should be fully considered in the HLD section in the Linxia Basin because the abundant paleosols throughout the section suggest significant floodplain weathering with soil development. This type of secondary weathering also exerts a dominant control on the eolian material weathering on the CLP. The total duration time for weathering profile development in both the catchment and deposition areas (e.g., the floodplain in the HLD section or the eolian accumulation area on the CLP) should be considered one of the major factors controlling the smectite/(illite + chlorite) ratio. It is reasonable to exclude the impact of transport between the source area and the deposition area because the transport in the two study regions was insufficient for silicate weathering. For the HLD section sediments in the Linxia Basin, the fluvial transport paths from the catchment (the west Qinling Mountains, as suggested by the unique northeastward paleocurrent during the Neogene, Fang et al., 2016) to the basin were quite short (a few tens of kilometers), and for the eolian sediments settling in the Linxia Basin or on the eastern CLP, the climate of the source area and the pass-through area was normally arid (An et al., 2001; Guo et al., 2002), and the transfer by wind was quick.

5.2. Intensified Weathering in the East Asian Monsoon Region

Before ~8 Ma, the SWI in the Linxia Basin was less variable, indicating a relatively stable regime in terms of uplift and denudation. This conclusion is supported by the generally low sedimentation rate (Figure 3d, Fang et al., 2016) and the stable provenance evidenced by the low degrees of variability in the bulk Nd isotopic values in the Linxia Basin (Figure 3e). With an increase in the sedimentation rate at ~8 Ma in the Linxia Basin (Figure 3e), a slight provenance change is suggested by the bulk Nd isotope data (Figure 3f) (Y. Yang et al., 2017). The SWI since ~8 Ma in the Linxia Basin cannot be explained by provenance changes. First, the paleocurrent direction measured from the two conglomerate layers where two kinds of fossil mammals are found in the HLD section (Figure 2) and the nearby LG section (Figure S1) indicate an unambiguously dominant southeasterly flow direction from ~12 to ~6 Ma, which is consistent with the dominant southeasterly flow over the Neogene across the Linxia Basin (Figure S1, Fang et al., 2016). The paleocurrent analyses thus suggest a dominant source in the southwest delivering materials into the basin by river, which may confirm a relatively steady provenance regime for river transport at ~9–8 Ma. Instead, the carbonate Sr-Mg-Ca elemental concentrations and Sr isotopes in the HLD section imply that such provenance change at ~8 Ma may have been caused by the extrabasinal eolian dust input by strong westerlies and/or East Asian winter monsoon (Y. Yang et al., 2017). In this regard, a generally drier climate in the upwind region seems likely to yield wind-blown dust with less weathered material into the Linxia Basin, which is inconsistent with the concurrent rise in the SWI. Moreover, a recent study in the Xining Basin, ~200 km northwest of the Linxia Basin (Figure 1b), has shown that the provenance control on SWI indices seems remarkable for various element ratio-based indices, even in the <2 μm fraction but has less of an impact on clay mineral assemblages (Yang et al., 2019). The limited impact of the provenance on the clay mineral assemblage may

Figure 3. Age profile of (I/S + smectite)/(illite + chlorite) ratios for the study sections and its comparisons with other records. (a–c) (I/S + smectite)/(illite + chlorite) ratios for the HLD section in the Linxia Basin and the CN section in the eastern CLP as well as the Na_2O/Al_2O_3 ratio for the CN section in our study; (d) change-point analysis (W. Taylor, 2000) of (I/S + smectite)/(illite + chlorite) ratios for the HLD section at ~9–7 Ma. (e) Sedimentation rates in the HLD section (Fang et al., 2016) and the CN section (Song et al., 2001); (f) ε_{Nd} values of the bulk sediments in the HLD section in the Linxia Basin (Y. Yang et al., 2017) and those of the bulk samples of the Lingtai (LT) eolian section on the CLP (Figures 1b, Z. Chen & Li, 2013). The change-point analysis in (d) shows that a significant clay ratio change from 1.2 to 2.1 occurred at 7.86 Ma (within a 95% confidence range of 7.8–8.1 Ma) with 100% confidence. The yellow shaded area marks the increase in the (I/S + smectite)/(illite + chlorite) ratios at ~9–7 Ma, and the gray bold line marks the boundaries of Pliocene/Quaternary and Loess-paleosol/Red Clay at ~2.6 Ma. CLP, Chinese Loess Plateau; CN, Chaona; HLD, Heilinding.

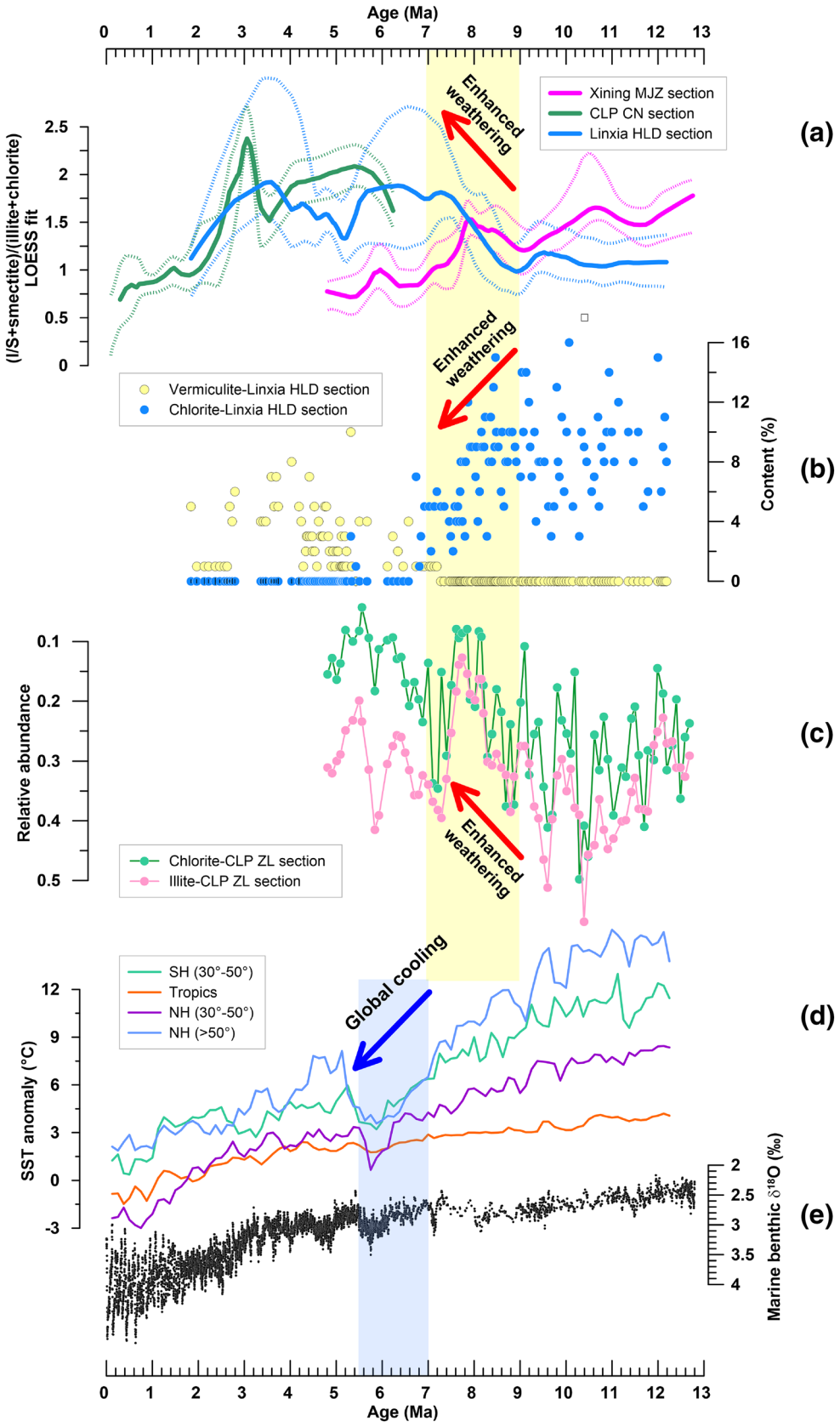
Age (Ma)
0 1 2 3 4 5 6 7 8 9 10 11 12 13
Enhanced weathering
Xining MJZ section
CLP CN section
Linxia HLD section
(a)
(I/S+smectite)/(illite+chlorite) LOESS fit
2.5 2 1.5 1 0.5 0
Enhanced weathering
Vermiculite-Linxia HLD section
Chlorite-Linxia HLD section
16 12 8 4 0
Content (%)
(b)
Relative abundance
0.1 0.2 0.3 0.4 0.5
Chlorite-CLP ZL section
Illite-CLP ZL section
Enhanced weathering
(c)
Global cooling
SH (30°-50°)
Tropics
NH (30°-50°)
NH (>50°)
SST anomaly (°C)
12 9 6 3 0 -3
(d)
2 2.5 3 3.5 4
Marine benthic δ18O (‰)
(e)
0 1 2 3 4 5 6 7 8 9 10 11 12 13
Age (Ma)

Figure 4.

be explained by the fact that the main parent minerals of newly formed clays (e.g., feldspars and micas) are widespread in various lithologies of the upper continental crust. The clay mineral distributions in modern soils globally and in China also support first-order climatic control (Chamley, 1989; Y. Xiong & Li, 1990). In addition, given the provenance change at ~8 Ma in the Linxia Basin, however, an input of recycled materials with a high SWI transported by river or by wind should also be considered because those materials may lead to an apparent rise in the (I/S + smectite)/(illite + chlorite) ratio in the HLD section. The (I/S + smectite)/(illite + chlorite) ratio in the MJZ section in the Xining Basin shows a significant decrease and generally becomes lower than those in the Linxia Basin at ~8 Ma (Figure 4a, Yang et al., 2019). Xining and Linxia Basins are both subbasins of a larger Paleocene-Miocene basin complex named the Longzhong Basin in the eastern portion of the northeastern TP (Zhai & Cai, 1984); thus, they generally share similar geological settings. Both basins have also experienced a large amount of extrabasinal eolian dust input since at least ~8 Ma (Ruan et al., 2019; Y. Yang et al., 2017). If recycled materials with a high SWI have dominated over the region since ~8 Ma, a concurrent rise of (I/S + smectite)/(illite + chlorite) ratios in the Xining and Linxia Basins can occur. However, a decrease in (I/S + smectite)/(illite + chlorite) ratios and the overall lower values of the ratios in the Xining Basin than those in the Linxia Basin since ~8 Ma suggest that the sediments in the HLD section sourced either from the catchment or extrabasinal dust are composed of rare recycled materials with a high SWI.

Considering the abundant soil development in the floodplain in the HLD section, we assume that the changes in the upper and lower envelopes of (I/S + smectite)/(illite + chlorite) (Figure 3c), as a first-order approximation, correspond to changes in the SWI in the deposition area (floodplain) and catchment (mountain range), respectively. Thus, the consistent increase in the SWI for the floodplain and mountain range from ~9 to 7 Ma in the Linxia Basin could be recognized as a combination of the concurrent strengthening of silicate alteration in the deposition area and in the catchment. This is not surprising because the catchment of the Linxia Basin is relatively small, and thus, the source and sinks are generally in the same hydroclimate. The finding of enhanced silicate weathering is also evidenced by the gradual disappearance of chlorite at ~9–7 Ma and the subsequent appearance of vermiculite (Figures 2 and 4b). Because vermiculite is a common alteration product of chlorite, we favor the explanation that enhanced weathering accounted for this change. A provenance change in which a source of fresh eroded chlorite became unavailable at ~9–7 Ma in the Linxia Basin seems unlikely since chlorite is widely seen in the less humid Xining Basin at 12–5 Ma (Yang et al., 2019) to the northwest of the Linxia Basin and the more humid western CLP at 12–5 Ma (Figure 4c) and eastern CLP at 6.2–2.6 Ma (Figure 2) to the southeast of the Linxia Basin. Given the significant tectonic activity in the northern TP at ~8 Ma (e.g., Lease et al., 2007; J. Li et al., 2014; Saylor et al., 2018; D. W. Zheng et al., 2006), the rapid exhumation corresponding to mountain uplift at ~8 Ma in the Linxia Basin (Fang et al., 2016) may yield an overall enhanced erosion rate in the catchment, which can shorten the weathering duration and thus reduce the SWI. However, this potential erosion-induced SWI decrease is overwhelmed by the climate-induced SWI increase. The increase in the SWI in the fluvial HLD section in the Linxia Basin also corresponds to a decrease in physical weathering proxies based on the increase in relative amounts of chlorite and illite in the eolian ZL section in the western CLP since ~8–9 Ma (Figure 4c; Y. Sun et al., 2015). Magnetic mineral and evaporite records in the Qaidam Basin on the northeastern TP and magnetic susceptibility in the western CLP also confirm a wetter period at ~8.5–7 Ma (Nie, Garzione, Su, Liu, & Zhang, 2017). Clay records in both the HLD fluvial and ZL eolian sections clearly suggest climate-enhanced silicate weathering since ~9–8 Ma that could be well correlated at a regional scale, which

Figure 4. Silicate weathering intensity evolution in the northeastern TP and the CLP. (a) Variations in the ratio of (I/S + smectite)/(illite + chlorite) in the HLD section in the Linxia Basin, the CN section in the eastern CLP and the MJZ section in the Xining Basin as shown by the locally weighted scatterplot smoothing (LOWESS, smoothing factor = 0.15, Cleveland, 1979) fittings through individual data point data (Data set S1); (b) the contents of chlorite and vermiculite in the HLD section; (c) relative abundances of chlorite and illite (chlorite/quartz and illite/quartz ratios) in the Zhuanglang (ZL) eolian section on the western CLP; (d) the stacked sea surface temperature (SST) anomalies for the Northern Hemisphere (NH), Southern Hemisphere (SH) and tropics (Herbert et al., 2016), and (e) marine) benthic oxygen isotope values (Zachos et al., 2001). Note that the dashed lines in (a) denote the error envelopes of the LOESS fittings. The yellow and blue shaded areas mark enhanced silicate weathering in the East Asian monsoon region at ~9–7 Ma and global cooling at ~7–5.4 Ma, respectively. CLP, Chinese Loess Plateau; CN, Chaona; HLD, Heilinding; TP, Tibetan Plateau.

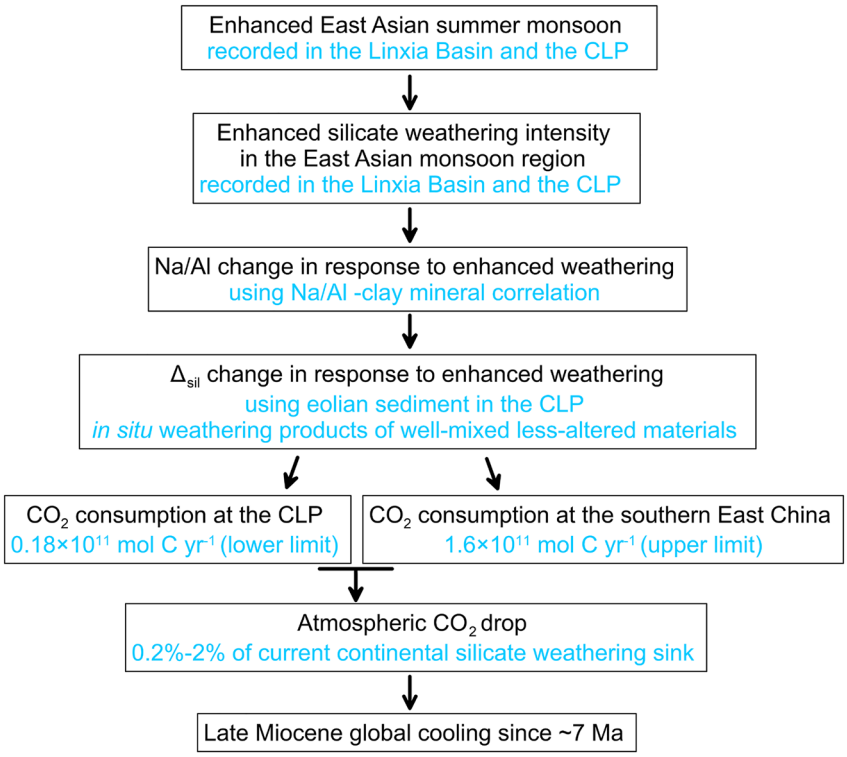

Figure 5. Schematic diagram showing our proposed new carbon sink mechanism that may have driven late Miocene global cooling. The blue text in the boxes shows the results of our study.

implies a greatly enhanced EASM since ~9–8 Ma because the EASM provides a majority of the moisture for the study region.

In principle, the primary factors controlling late Miocene development of the East Asian monsoon climate are global cooling (e.g., Miao et al., 2011), Antarctic glaciation (Ao et al., 2016) and the tectonic uplift of the TP (e.g., An et al., 2001; Tada et al., 2016; Zoura et al., 2019), especially the rise and growth of the northern TP, as revealed by climate models (e.g., An et al., 2001; Tada et al., 2016; R. Zhang et al., 2012). The driving force of the significantly enhanced EASM is unlikely to be global cooling, which should have weakened the SWI. The progress of Antarctic ice sheet growth has been previously proposed to explain the long-term magnetic enrichment of eolian deposits, especially the significant enrichment since ~ 6 Ma in the CLP (e.g., Ao et al., 2016). However, this mechanism also seems unlikely because the ice sheet in western Antarctica formed at ~6 Ma (Zachos et al., 2001), which is significantly later than the onset of the enhanced East Asian monsoon systems at ~9–8 Ma (see records in Figures 4b and 4c). The uplift and growth of the northern and eastern parts, and even the entirety, of the TP approximately 8–9 Ma have been widely reported (e.g., Lease et al., 2007; J. Li et al., 2014; Molnar, 2005; Saylor et al., 2018; D. W. Zheng et al., 2006). In particular, the uplift of the northern TP could significantly enhance the EASM circulation, thus extending the monsoon front farther inland and strengthening the monsoon rainfall in the northern East Asian monsoon region (R. Zhang et al., 2012). This uplift-induced EASM enhancement is mainly caused by the surface sensible heating of the northern and central TP that can induce a low-level cyclonic anomaly around the TP, thus strengthening the northward advance of warm advection from the south of the TP (Tang et al., 2013). The dominance of the uplift of the TP on the formation of a modern-like climate regime in East Asia is also supported by a recent climate modeling study (Zoura et al., 2019), which highlighted that the primary control on the Asian hydroclimate is the topography of the TP rather than CO_2 changes and ice sheet formation, although the latter two factors are also important (R. Zhang et al., 2018). Thus, the increases in the SWI in the HLD and ZL sections at ~9–7 Ma suggest a significant uplift-forced intensification of the EASM (Figure 5)

It should be noted here that an enhanced EASM, as documented in the Linxia Basin and the eastern CLP region at ~9–7 Ma, does not conflict with the records of regional drying (e.g., Jiuxi Basin, Ma et al., 2005; Xining Basin, Yang et al., 2019) and dust deposition (Linxia Basin, M. Fan et al., 2006; Y. Yang et al., 2017; CLP, Qiang et al., 2001; Song et al., 2001) because the uplift of the northern TP has also facilitated Asian inland drying and Asian dust emission and transport (e.g., Ruddiman & Kutzbach, 1990; X. D. Liu & Dong, 2013; Y. Sun et al., 2015; H. Sun & Liu, 2018). For example, the synchronous increases in the SWI (Figure 4a) and dust input in the Linxia Basin (Y. Yang et al. 2017) at ~8 Ma suggest a synchronous intensification of the EASM-derived moisture and the EAWM or westerlies-derived dust settling, which can reasonably be regarded as the environmental consequence of the TP uplift. Moreover, on a regional scale, the regional clay records of the SWI in the Linxia and Xining Basins show a divergent evolution since ~8 Ma (Figure 4a). This regional weathering contrast (Figure 4a) can be explained from a perspective that invokes the effects of mountain range uplift on both erosion and climate (Figure S6) as follows: 1) precipitation increases on the windward side and decreases on the leeward side of a mountain located on the moisture path and 2) strong erosion in tectonically active regions results in a lower SWI of eroded materials. Specifically, the intensified precipitation on the CLP and the windward side of the northeastern TP is thus assumed to be caused by the enhancement of the EASM, and this increase in precipitation would have induced enhanced pedogenesis and strong silicate weathering on the CLP and Linxia Basin. Notably, the Linxia Basin is open eastward to the west of the CLP, allowing monsoon moisture penetration (Figure 1b). However, the monsoon precipitation in the Xining Basin may have decreased greatly because of the high mountain barrier located along the path of the monsoon (e.g., the rapid uplift of the Laji and Jishi Mountains between the Linxia and Xining Basins ~8 Ma, Lease et al., 2007; Saylor et al., 2018), potentially causing a drying trend in the Xining Basin. On the other hand, the tectonic uplift along with rapid erosion caused a lower degree of weathering profile development in the catchment areas of the Linxia and Xining Basins, resulting in a weaker alteration of silicate minerals. This tectonic-derived erosion effect may be pronounced in the Xining Basin but overwhelmed by the increase in monsoon precipitation in the Linxia Basin, regardless of an increase in the sedimentation rate (Figure 3e), as mentioned. Such topography-induced hydroclimate divergence is also documented in the Pamir region, where distinct west-east hydroclimate differences were established during the late Oligocene when the relief of the Pamir-Tian Shan is higher than 75% of the modern elevation (Wang et al., 2020).

5.3. Enhanced CO_2 Consumption in the CLP

The increase in the SWI in the Linxia Basin in the western CLP and the northeastern TP at ~9–7 could be regarded as a weathering response to the significantly enhanced EASM over East Asia. To obtain a first-order estimate of the long-term CO_2 consumption flux associated with the enhanced silicate weathering flux, the CO_2 consumption increase per unit weight material associated with this enhanced silicate weathering (Δ_{sil}, mol C kg^{-1}) should first be assessed. Δ_{sil} can be determined from the difference in the soil composition in the areas impacted by monsoon enhancement at ~8 Ma. However, Δ_{sil} cannot be directly evaluated by the chemical composition of the HLD fluvial sediments because the bulk chemical compositions of these fluvial sediments are dominantly influenced by the frequently altered sedimentary facies with distinct grain sizes (Figure 2) instead of by catchment weathering alone. The best method for determining regional silicate depletion is to use the eolian Red Clay sequence over the eastern CLP because this Red Clay mainly represents *in situ* weathering of wind-blown material with relatively uniform bulk mineral and chemical compositions and a stable sedimentation rate. Given that plagioclase and K-feldspar and mica minerals are the main parent minerals for silicate weathering in the eolian CN section (Figure S3), the weathering of plagioclase (An_{20}) and precipitation of secondary clay minerals (kaolinite) via water and soil CO_2 (Winnick & Maher, 2018) could be represented by

$$1.66Ca_{0.2}Na_{0.8}Al_{1.2}Si_{2.8}O_8 + 2CO_2(g) + 3H_2O \leftrightarrow Al_2Si_2O_5(OH)_4 + 0.33Ca^{2+} + 1.33Na^{+} + 2.66SiO_2(aq) + 2HCO_3^{-} \quad (1)$$

Similarly, the K-feldspar weathering to kaolinite could be represented by

$$2KAlSi_3O_8 + 2CO_2(g) + 3H_2O \leftrightarrow Al_2Si_2O_5(OH)_4 + 2K^{+}4SiO_2(aq) + 2HCO_3^{-} \quad (2)$$

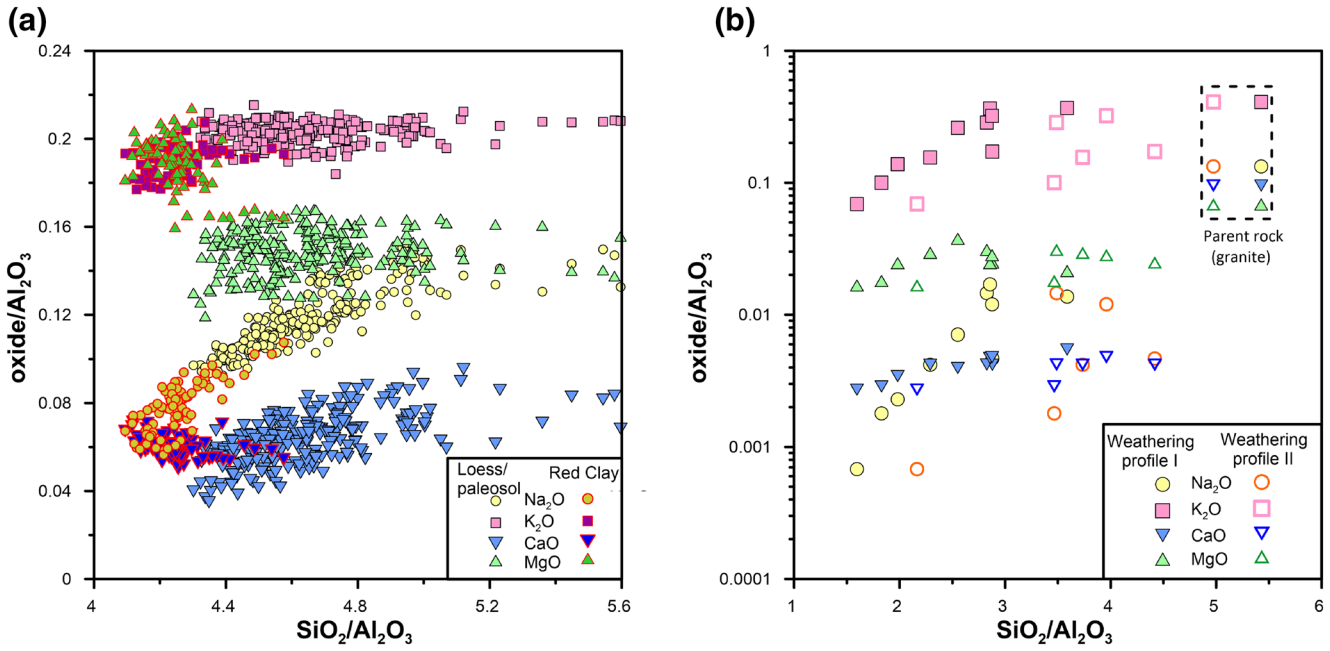

Figure 6. Correlation between oxide/Al_2O_3 and the well-used index of silicate weathering intensity (SiO_2/Al_2O_3) in modern and paleo-weathering profiles. (a) Loess/paleosol and Red Clay sequences on the eastern Chinese Loess Plateau (CLP) (data from S. Xiong et al., 2010) and (b) granite weathering profiles in southern East China (data from Fu et al., 2019). Note that K, Na, Ca, and Mg all exhibit uniform depletion with increasing weathering intensity (increases in SiO_2/Al_2O_3) in the weathering profiles but show complex gain/loss patterns in the loess/paleosol and Red Clay sequences.

The muscovite weathering to kaolinite could be represented by

$$2KA1_3Si_3O_{10}(OH)_2 + 2CO_2(g) + 5H_2O \leftrightarrow 3Al_2Si_2O_5(OH)_4 + 2K^+ + 2HCO_3^- \quad (3)$$

It should be noted that there are several ways of expressing these reactions. The above three examples are highly generalized because of the complex nature of feldspars and clay minerals and the formation of many intermediate minerals within various environmental conditions. For example, in the less humid CLP region, K-feldspar may not directly degrade into kaolinite due to the limit of water availability and probably transform to muscovite:

$$3KAlSi_3O_8 + 2CO_2(g) + 2H_2O \leftrightarrow KAl_3Si_3O_{10}(OH)_2 + 2K^+ + 6SiO_2(aq) + 2HCO_3^- \quad (4)$$

Regardless of the complexities during silicate weathering, for any silicate weathering reaction in the upper crust, the amount of long-term atmospheric CO_2 consumption could be quantitatively estimated by the amount of base cation depletion in primary minerals (e.g., Ca, Na, K, and Mg). For Equations 1–4, 2 mol of CO_2 are consumed in all reactions but 1 mol of CO_2 will be returned to the ocean-atmosphere system during carbonate precipitation in the ocean, thus only 1 mol of CO_2 is finally buried via silicate weathering at the geological timescale. Δ_{sil} can therefore be calculated based on stoichiometry from the overall difference in the Red Clay base cations before and after monsoon-enhanced silicate weathering at ~8 Ma, that is, $\Delta_{sil} = \Delta Ca + \Delta Mg + \Delta K + \Delta Na$. This method is based on differences in the ratios of the major cations to Al_2O_3 following France-Lanord and Derry (1997) and assumes that Al is stable during weathering.

The validity of the Δ_{sil} calculation depends on the assumption that stronger silicate weathering will lead to a greater depletion of base cations. This assumption is always true within modern weathering profiles. As seen in modern granite weathering in southern East China (Fu et al., 2019), the degree of base cation depletion (oxide/Al_2O_3) is positively correlated with the SWI indices (e.g., SiO_2/Al_2O_3, Ruxton, 1968) (Figure 6b). However, this relationship is not always observed in sedimentary profiles, even in the *in situ* weathering archives of Red Clay and loess/paleosols. For example, a close examination of the bulk composition of

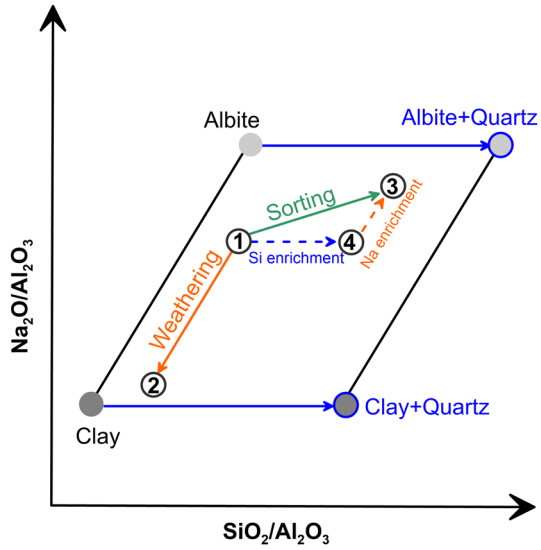

Figure 7. Schematic diagram of Na_2O/Al_2O_3 versus SiO_2/Al_2O_3 showing the weathering and sorting effects on the chemical composition of eolian sediments. A weathering trend resulting from the transformation of albite to clay can be illustrated by the orange arrow from circle 1 to circle 2, which is parallel to the albite and clay connection. The addition of quartz yields an increase in SiO_2/Al_2O_3 but no change in Na_2O/Al_2O_3, as shown by the bold blue arrow. Strong wind sorting (solid green arrow from circle 1 to circle 3) can be regarded as a combined result of an addition of quartz (Si enrichment, dashed blue arrow from circle 1 to circle 4) and a decrease in clay content (Na enrichment, dashed orange arrow from circle 4 to circle 3). The Na/Si enrichment ratio can thus be used to estimate the magnitude of the sorting effect on Na_2O/Al_2O_3 ratio changes.

eolian Red Clay and the loess/paleosol sequence in the nearby BS section in the eastern CLP (Figure 1, S. Xiong et al. 2010) reveals that this relationship is only obvious for Na, less obvious for K, and undetectable or even inverted for Ca and Mg (Figure 6a). These findings suggest that a simple calculation using the overall difference in the chemical composition (including Na, K, Ca and Mg) between the Red Clay and parent rock cannot yield a reliable Δ_{sil}. The Na_2O/Al_2O_3 ratio in the Red Clay and loess/paleosol sequence exhibits a coherent and uniform evolution with SiO_2/Al_2O_3 (Figure 6a), regardless of the potential effects of differences in provenance and diagenesis between the two types of eolian sequences (loess/paleosol and Red Clay). The Na_2O/Al_2O_3 ratio is thus suggested to be a suitable tool to scale Δ_{sil} (Figure 5).

However, SiO_2/Al_2O_3 can not only mirror silicate depletion during the weathering profile, as demonstrated above but can also trace the sorting effect (normally with quartz enrichment), as shown by the excellent relationship between SiO_2/Al_2O_3 and median grain size ($r^2 = 0.91$, $n = 319$, S. Xiong et al., 2010). Therefore, the sorting effect on the Na_2O/Al_2O_3 ratio needs to be considered before using this ratio to estimate Δ_{sil}. We have developed a bivariate graph of Na_2O/Al_2O_3 versus SiO_2/Al_2O_3, which could reveal the changes in the relative proportions of these elements within albite, clays and quartz (Figure 7). Because albite is the only Na-bearing silicate mineral that can be weathered in the eolian sequences at the CLP (Figure S3), we assume that weathering can only induce the transformation of albite into clay and that the proportion of quartz remains constant due to its high stability. Strong wind sorting results in an increase in the relative proportions of quartz to albite since albite is less stable during transport and a decrease in the clay proportion due to grain size differentiation. Thus, for a parent rock with a given proportion of these three minerals (circle 1 in Figure 7), the transformation of albite into clay yields a clear weathering trend (see weathering reaction Equation 1 characterized by Na depletion and Al enrichment; arrow from circle 1 to circle 2). Strong winds can result in an obvious sorting trend (arrow from circle 1 to circle 3) characterized by an increase in the quartz proportion due to its high stability (Si enrichment, arrow from circle 1 to circle 4) and a decrease in the clay proportion relative to albite (Na enrichment, arrow from circle 4 to circle 3). The Na_2O/Al_2O_3 ratio change caused only by the sorting effect can be measured by the change magnitude of Na enrichment relative to that of Si enrichment (Figure 7).

We use our constructed model to analyze the sorting effect on the Na_2O/Al_2O_3 ratio in the eolian sequence in the CLP (S. Xiong et al., 2010). For loess/paleosol samples with high SiO_2/Al_2O_3 ratios >~4.9, a weak change in the Na_2O/Al_2O_3 ratio is observed. In contrast, for the loess/paleosol samples with SiO_2/Al_2O_3 < ~4.9, a significant inverse relation between SiO_2/Al_2O_3 and Na_2O/Al_2O_3 is observed (Figure 8), and this relation can be extrapolated to encompass all Red Clay samples. Furthermore, the K_2O/Al_2O_3 ratios of all loess/paleosol and Red Clay samples also display a two-stage trend involving a relatively stable trend when SiO_2/Al_2O_3 > ~4.3 (mostly loess/paleosol samples) and an inverse relation between SiO_2/Al_2O_3 and Na_2O/Al_2O_3 when SiO_2/Al_2O_3 < ~4.3 (mostly Red Clay samples). However, the inverse relation for SiO_2/Al_2O_3 versus K_2O/Al_2O_3 occurs at a SiO_2/Al_2O_3 ratio of ~4.3, which is considerably lower than ~4.9 for SiO_2/Al_2O_3 versus Na_2O/Al_2O_3. These observations indicate a very limited sorting effect on changes in the Na_2O/Al_2O_3 ratio. First, the inverse relations of SiO_2/Al_2O_3 versus K_2O/Al_2O_3 and Na_2O/Al_2O_3 that occur at distinct SiO_2/Al_2O_3 ratios can be well explained by the different weathering resistances of Na- and K-bearing minerals since Na-bearing plagioclase is more easily weathered than K-bearing potash feldspar and muscovite. This can also be indicated by the relation of SiO_2/Al_2O_3 versus Na_2O/K_2O, where Na_2O/K_2O ratios exhibit a consistent decrease with decreasing Na_2O/Al_2O_3 ratio when SiO_2/Al_2O_3 < ~4.9 but display a constant value when SiO_2/Al_2O_3 > ~4.9 (Figure 8). Such distinct patterns of Na-K differentiation clearly suggest a dominant impact of weathering rather than sorting on plagioclase/K-feldspar differentiation, as also indicated in

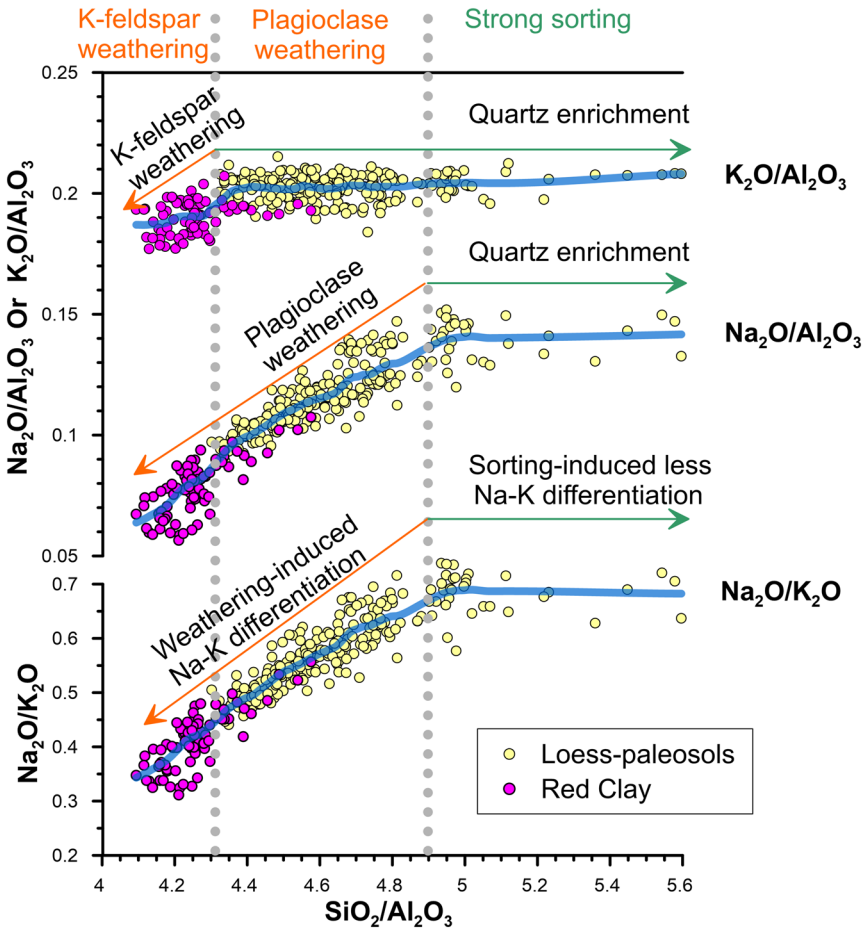

Figure 8. Distinguishing the sorting and weathering effects on chemical composition for the loess/paleosol and Red Clay sequences in the CLP. The bold blue lines denote the LOWESS fittings of those data, and the vertical dotted lines mark a break point at $SiO_2/Al_2O_3 = 4.32$ for the K_2O/Al_2O_3 data set and a starting point at $SiO_2/Al_2O_3 = 4.90$ for the obvious persistent decreases of Na_2O/Al_2O_3 and Na_2O/K_2O along with decreasing SiO_2/Al_2O_3 based on a change-point analysis (W. Taylor, 2000). Note that the nearly constant Na_2O/Al_2O_3, K_2O/Al_2O_3 and Na_2O/K_2O ratios when SiO_2/Al_2O_3 values are high suggest very limited Na_2O/Al_2O_3 and K_2O/Al_2O_3 changes and less Na-K differentiation during strong sorting, which corresponds to the high Si but low Na enrichment indicated in Figure 7. See details in the text.

previous studies investigating the effects of chemical weathering and sorting on bulk composition and mineralogy (e.g., Nesbitt & Young, 1996; Nesbitt et al., 1997). This is mainly due to the more ready alteration of plagioclase than K-feldspar, although both display near-identical hardness and cleavage properties (Nesbitt et al., 1997). Second, since strong winds always produce intense sorting, when a pronounced sorting effect is observed in samples with high SiO_2/Al_2O_3 ratios, the less changeable Na_2O/Al_2O_3 (Figure 8) suggests a very low magnitude of Na enrichment relative to Si enrichment (Figure 7). The low Na/Si enrichment ratios indicate that wind sorting in the eolian sequence in the CLP was dominantly characterized by a change in the proportion of quartz relative to the proportions of other silicates and by a very limited Na_2O/Al_2O_3 change. This profound sorting effect is mainly linked to the degree of quartz enrichment, which was evidenced by the uniform grain size parameters derived from the bulk and quartz samples from the loess/paleosol sequences (Y. Sun et al., 2006). Instead, a comparison of the grain size parameters of the bulk and quartz samples from the Red Clay sequence that formed in more humid settings reveals distinct results. The distinct grain size parameters of the bulk and quartz samples in the Red Clay sequence indicate more pronounced pedogenic processes (Y. Sun et al., 2006), suggesting that weathering rather than sorting is more important in controlling the geochemistry of eolian sediments.

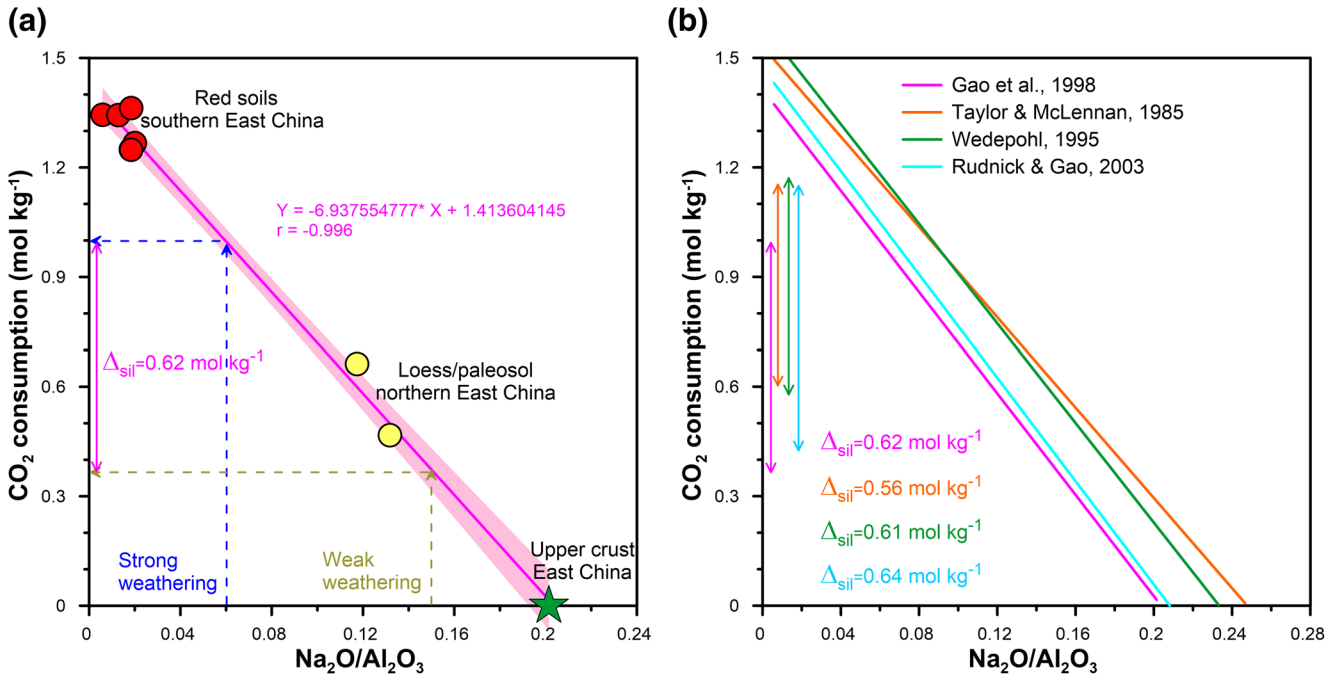

Figure 9. Correlation between Na_2O/Al_2O_3 and CO_2 consumption in the parent rock endmember and soils. (a) Correlation between Na_2O/Al_2O_3 and CO_2 consumption for loess and paleosol samples in northern East China and three average compositions of typical red soil datasets in southern East China. The upper crust composition of central East China (S. Gao et al., 1998) is chosen as the parent rock. The loess and paleosol data are from the carbonate-free samples from the uppermost Pleistocene loess and paleosol samples in the Xifeng (XF) section (Figure 1b; number XFC85 and XFC149 in Liang et al., 2009). The red soil data are from typical Quaternary red earth datasets along the Yangtze River (Figure 1; J. X. Zhang et al., 2007; Hong et al., 2013) and average compositions of the three subtypes of red soils covering all of southern China, including red earth, yellow earth and laterite (CNEMC, 1990). These data form an excellent fit line with 95% confidence (pink shading area). The difference in CO_2 consumption (Δ_{sil} = 0.62 mol kg^{-1}) between a relatively weak weathering stage (olive dashed line) and a strong one (blue dashed line) can thus be estimated by the upper and lower limits of the Na_2O/Al_2O_3 ratios in the eolian sequence (e.g., the Na_2O/Al_2O_3 ratios of 0.15 and 0.06 in the BS section and 0.13 and 0.04 for the CN section, respectively) (see Figure 10). (b) Test of the dependence of Δ_{sil} on the parent rock composition using different upper crust compositions (S. Gao et al., 1998; Rudnick & Gao, 2003; S. R. Taylor & McLennan, 1985; Wedepohl, 1985). The bold lines show linear fits for loess/paleosol and Red Clay data based on different parent rock compositions; the related parameters for each fit can be seen in Tables S3 and S4. Double-headed arrows mark the Δ_{sil} values derived from the difference in CO_2 consumption using Na_2O/Al_2O_3 ratios of 0.15 and 0.06 in the BS section for each parent rock endmember. BS, Baishui; CN, Chaona.

After excluding the sorting effect, we then reconstructed the Na_2O/Al_2O_3 ratio versus Δ_{sil} relationship for typical soils based on the composition difference between soils and parent rocks in East China (Table S2). The data are based on the chemical compositions of typical latest Pleistocene loess and paleosol samples in the CLP (Figure 1, Liang et al., 2009), the three typical Quaternary red soil datasets along the Yangtze River (Figure 1, DTL, n = 123; JJ, n = 44; XC, n = 18) (Hong et al., 2013; J. X. Zhang et al., 2007), and the average compositions of the top A horizon of three subtypes of red soils (red earth, 77 locations; yellow earth, 37 locations; and laterite, 7 locations; CNEMC, 1990) covering the entirety of southern China. The upper crust composition of central East China (termed "CEC" in S. Gao et al., 1998; includes the Yangtze craton, the North China craton and the Qinling orogen between these cratons) was calculated by averaging the exposed rock types according to their thickness and exposure area and includes sedimentary cover and the underlying metamorphosed crystalline basement. The CEC composition is thus the best candidate for representing the average compositions of parent rocks exposed within the critical zone over this broad region. The constructed Na_2O/Al_2O_3 ratio and Δ_{sil} relationship exhibit an excellent linear distribution (correlation coefficient, $r = -0.996$ for a linear fit) (Figure 9a), suggesting a wide usability for Δ_{sil} estimation.

We further assessed the correlation of the two silicate weathering indices Na_2O/Al_2O_3 and (I/S + smectite)/(illite + chlorite) (Figure 5). The Neogene rapid uplift of the northeastern TP is thought to have played a critical role in the generation and transport of riverine detritus into adjacent fluvial basins (S. Liu et al., 2019) or of eolian dust to the downwind CLP (e.g., Bird et al., 2020; Z. Chen and Li, 2013). For the latter case, reworked Yellow River-derived northeastern TP sediments or old loess deposits provide a major eolian supply

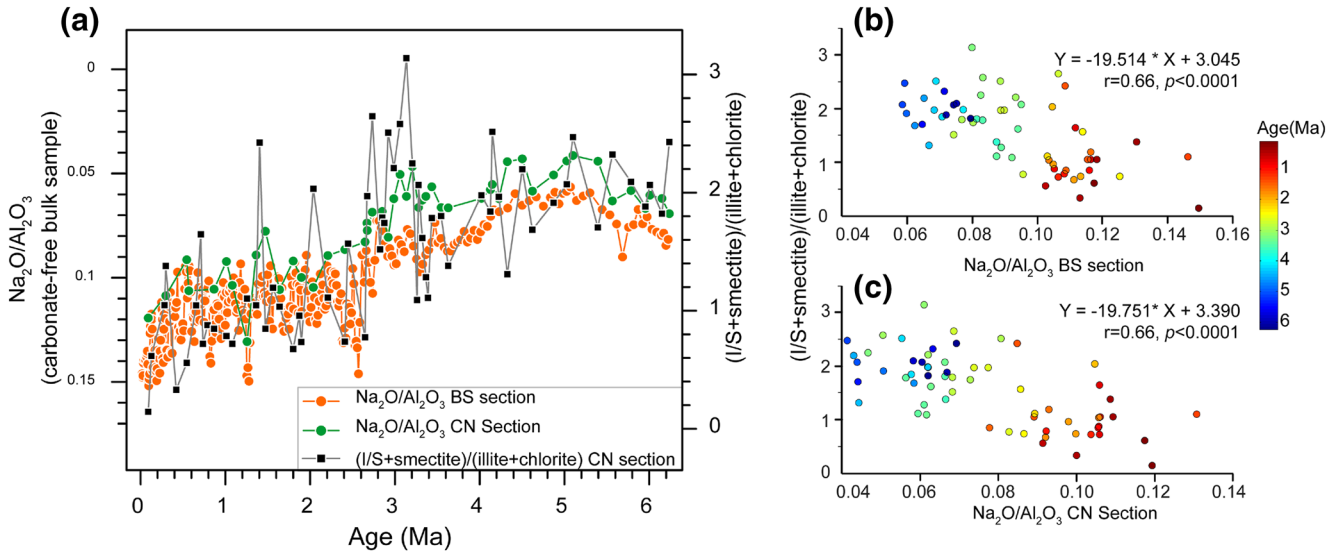

Figure 10. Comparison of the Na_2O/Al_2O_3 ratio of bulk samples with clay assemblages in the eolian sections on the CLP. (a) Age profiles of the Na_2O/Al_2O_3 ratio of carbonate-free bulk samples in the BS (S. Xiong et al. 2010) and CN sections (this study) with the (I/S + smectite)/(illite + chlorite) ratio in the CN section (this study). (b) and (c) Correlations of the Na_2O/Al_2O_3 ratio of carbonate-free bulk samples and (I/S + smectite)/(illite + chlorite) ratio in the CN and BS sections. The Na_2O/Al_2O_3 data in (b) and (c) were interpolated with the same sample resolution of the clay mineral data. BS, Baishui; CLP, Chinese Loess Plateau; CN, Chaona.

of the CLP (e.g., Licht et al., 2016; Nie et al., 2015). The roughly same provenance regime and the consistent evolution and value range of the (I/S + smectite)/(illite + chlorite) ratio between the CN and HLD sections since 6.2 Ma (Figure 3a), may suggest a comparable degree of silicate depletion between the western and eastern CLP regions. The magnitude of change in the (I/S + smectite)/(illite + chlorite) ratio between 9 and 7 Ma in the HLD section could therefore be roughly the same as that of the clay ratio for the entire CN Red Clay and loess/paleosol sequences (Figures 3a and 4a). Thus, the consistency between the (I/S + smectite)/(illite + chlorite) ratio and Na_2O/Al_2O_3 ratios within the Red Clay and loess/paleosol sequence (Figure 10) suggests that the variability in the Na_2O/Al_2O_3 ratio can be used to estimate that of the (I/S + smectite)/(illite + chlorite) ratio in both sections. This evaluation will yield a maximum value of Δ_{sil} because other potential effects (e.g., sorting, although this factor is insignificant as discussed above) may amplify the variability in the original Na_2O/Al_2O_3 ratio derived from *in situ* weathering.

The Na_2O/Al_2O_3 ratios in both the CN and BS sections correlate well with the (I/S + smectite)/(illite + chlorite) ratio in the CN section (Figures 10b and 10c), suggesting a regional consistency of SWI around the CLP region. The Na_2O/Al_2O_3 ratio in both eolian sections exhibits a difference of 0.09 between the minimum and maximum values (0.06 and 0.15 for the BS section and 0.04 and 0.13 for the CN section, respectively) (Figure 10a). Based on the reconstructed Na_2O/Al_2O_3 and Δ_{sil} relationship (Figure 9a), the Na_2O/Al_2O_3 difference yields a Δ_{sil} value of 0.62 mol C kg^{-1} (Figure 5). To test the dependence of the Δ_{sil} value on the parent rock composition, we also employed three commonly used values for the upper crust (Rudnick & Gao, 2003; S. R. Taylor & McLennan, 1985; Wedepohl, 1995) to generate additional Na_2O/Al_2O_3 and Δ_{sil} relationships (Figure 9b; Tables S3). The four different recommended values of the upper crust have Na_2O/Al_2O_3 values ranging from 0.20 to 0.26 and can effectively fit the loess/paleosol and data (with *r* values between −0.990 and −0.998). These endmembers produce a very narrow range of Δ_{sil} values between 0.56 and 0.64 mol C kg^{-1}, with a mean of 0.61 ± 0.3 mol C kg^{-1}, corresponding to the Na_2O/Al_2O_3 difference of 0.09 in the BS section (Table S4). The consistent Δ_{sil} values derived from these parent rock endmembers indicate that the Δ_{sil} estimate does not rely heavily on the parent rock endmember composition. Furthermore, based on the calculations using the four endmembers, the absolute CO_2 consumption values range from 0.37 to 0.6 mol C kg^{-1} for a Na_2O/Al_2O_3 value of 0.06 and from 1.00 to 1.18 mol C kg^{-1} for a Na_2O/Al_2O_3 value of 0.15 (the double-sided arrows in Figure 9b). Such relatively large differences in the absolute CO_2 consumption values from different endmembers further suggest that our Δ_{sil} calculation relies mainly on the

compositional difference produced by the degree of weathering intensity and not on the compositions of the parent rocks (which may have distinct Na/Al ratios in various upper continental settings), thus highlighting the validity of applying this Na/Al-based method to the broad East Asian region.

Given a median bulk density of 2 g cm^{-3} for the Red Clay (Y. Sun & An, 2002) and an average deposition rate of 2.3 cm kyr^{-1} for the Red Clay deposits in the CN section with less varied sedimentation rates in the section (Song et al., 2001, Figure 3), a total area of 6.4×10^{11} m^2 for the CLP and a calculated mean Δ_{sil} value of 0.61 mol C kg^{-1} yield a CO_2 consumption flux of 0.18×10^{11} mol C yr^{-1}. This amount of CO_2 consumption accounts for ~0.2% of the current continental silicate weathering sink (Figure 5; global CO_2 consumption rates from silicate weathering are 8.70×10^{12} mol C yr^{-1} from Gaillardet et al., 1999, or 7.85×10^{12} mol C yr^{-1} from a new analysis of Moon et al., 2014). The above estimate is based on the assumption that eolian material settled over an area covering the entire CLP at ~9–8 Ma. This assumption is reasonable since the complete Quaternary loess-paleosol sequence is commonly underlain by the eolian Red Clay formation in the eastern CLP (e.g., Ding et al., 2001; T. S. Liu, 1985) and even in the western CLP (e.g., Zan et al., 2018). Although there are generally poor preservation conditions for Red Clay accumulation in the western CLP where fluvial systems are fully developed in this tectonically active setting, a recent study suggests that a great amount of eolian material has settled in the Linxia Basin since ~9–8 Ma (Y. Yang et al., 2017). Here, the estimated CO_2 consumption flux of the CLP region should be considered as a lower limit for the northern part of the East Asian monsoon region (north of the Qinling Mountains-Huai River Line that marks the climatic boundary of the East Asian monsoon region, Figure 1a) because the tectonically active western CLP adjacent to the northeastern TP at ~8 Ma can provide more materials subjected to weathering than the eastern CLP.

5.4. The Upper Limit Estimate of CO_2 Consumption in Southern East China

Although the eolian Red Clay and loess/paleosol sequence is mainly located in the eastern CLP, it provides a unique case for directly evaluating the paleo-weathering profile changes in response to the monsoon climate throughout East Asia because it has not experienced any re-mobilization (e.g., Guo et al., 2001). Here, we underline the potential wide applicability of the eolian composition at the CLP to the assessment of regional weathering conditions because many controversial records linked to the Asian monsoon and weathering conditions are reconstructed by sediments that are transported to the final deposition site after weathering. The fine-grained eolian sediments in the CLP are well-mixed less-altered materials from a broad semi-arid and arid region that have been further weathered in the CLP region, thus yielding an invaluable archive of *in situ* weathering conditions mainly driven by monsoon precipitation.

Before the Δ_{sil} value derived from the eolian sequence can be applied to the monsoon region in southern East China (south of the Qinling Mountains-Huai River Line, Figure 1a), we need to further consider factors that are essential to the weathering comparability between the two regions, such as lithology of parent rock and soil residence time. First, for the lithology of parent rock, there is a generally good correspondence of major elements between various independent estimates of the composition of upper continental crust globally (Rudnick & Gao, 2003), suggesting a relatively constant major elemental and mineralogical composition over a large spatial scale. The relationship between the estimated Δ_{sil} versus Na_2O/Al_2O_3 in various upper continental crust endmembers (Figure 9b) indicates that Δ_{sil} relies less on the elemental compositions of a specific parent rock but more on the change in the magnitude of silicate depletion. In addition, major and trace elemental features of the Red Clay and loess/paleosols are also identical to those of upper continental crust (e.g., Ding et al., 2001), suggesting that the Δ_{sil} value derived from the CLP can be used to estimate the large-scale bedrock weathering in southern East China. Second, for the soil residence time that is mainly controlled by the sedimentation rate of eolian deposits in the CLP and bedrock denudation rate in southern East China, the southern East China and eastern CLP regions are both generally characterized by topographically low and tectonically stable regions relative to the TP during the late Cenozoic. In particular, the ^{10}Be-based erosion rate varies from 2 to 5 cm kyr^{-1} in low-elevation areas in South China (Chappel et al., 2006), which is within a similar range of sedimentation rates as the eolian sequence on the CLP, 1–3 cm kyr^{-1} for Red Clay and 6–8 cm kyr^{-1} for loess/paleosols in the CN section.

Given the available weathering comparability, however, the enhanced EASM at ~8 Ma, as suggested by our records in the CLP and northeastern TP in the northern East Asian monsoon region, is contradicted by the sedimentary archives in the South China Sea (Clift et al., 2014; Wan et al., 2007a). The less-altered material (with a low chemical alteration index but high chlorite and K/Al ratios) that appeared in the post-~8 Ma sediments in the South China Sea was previously assumed to be caused by a weakened EASM (Clift et al., 2014; Wan et al., 2007a, 2010), which is inconsistent with our SWI records. In an alternative view, however, the less-altered material might reflect a strong eolian input of high contents of illite and chlorite caused by the intensified East Asian winter monsoon since ~8 Ma rather than a weak EASM (Wan et al., 2007b), which can be supported by the enhanced Asian dust input into the Japan Sea (Shen et al., 2017) and North Pacific Ocean (Rea et al, 1998) since ~8 Ma. In addition, an enhanced EASM may also induce changes in erosion and transport regimes in the source-to-sink systems over southern East China, thereby leading to less-altered material accumulation in the South China Sea. In this scenario, however, such weakened weathering intensity may possibly occur with a higher erosion flux, thereby yielding net CO_2 consumption. Considering the above substantial uncertainties, the following estimates based on an assumption that the stronger EASM at ~9–7 Ma involves the entire southern East Asian monsoon region can be regarded as an upper limit of CO_2 consumption over southern East China.

Modern southern East China is characterized by exoreic drainages where erosional detritus is carried by rivers to the ocean. The erosion rates in this area exhibit a large range of between 250 and >1,000 t km^2 yr^{-1} (Walling & Webb, 1983). The >6,000 km long Yangtze River drains variable landscapes with different climates in southern East China, thereby providing an ideal basis for estimating the area-averaged erosion rate for the entire study area. Although how much bedload reaches the ocean is debatable, many large rivers presumably have very small bedloads compared to suspended loads (Milliman & Meade, 1983). We therefore assume that the suspended load produced over the broad study area, to the first-order, exhibits the same magnitude as that in the Yangtze drainage basin. The sediment suspended load of the Yangtze River was 0.48×10^{12} kg·yr^{-1} prior to the early 1980s (Milliman & Syvitski, 1992), providing an upper limit of the erosional flux over the Yangtze drainage basin when agricultural use is considered. Except for the delta plain and proximal subaqueous delta during the Holocene, the Yangtze River-derived sediment can be transported to an elongated (~800 km) distal subaqueous mud wedge. This distal mud wedge yields an annual sediment load of 2.4×10^{12} kg yr^{-1} for the past 7,000 years, which is approximately half the current annual Yangtze sediment discharge (J. P. Liu et al., 2007). Although the impact of agricultural use is hard to assess, the distal mud wedge, as one of the reservoirs of the Yangtze sediment, has yielded such a remarkably high sediment load, suggesting that the present sediment suspended load of the Yangtze River is a reliable approximation (within an order of magnitude) of that in a "natural" condition. This is contrary to the Yellow River drainage basin, where the Yellow River sediment load was an order of magnitude lower before humans began farming the loess hills of northern China (Milliman et al., 1987).

The present sediment suspended load of the Yangtze River can be extrapolated to the entire study area (including 15 provinces and autonomous regions of southern East China), with a total area of $\sim 2.6 \times 10^{12}$ m^2, ultimately yielding a suspended load of 0.66×10^{12} kg yr^{-1}. However, the sediment budget at ~8 Ma is not clear because, until now, the reconstructed late Cenozoic sediment budgets for the major basin systems of East Asia have yielded distinct results in terms of long-term change (Clift, 2006; Métivier et al., 1999) and glacial-interglacial variation during the Quaternary (Clift et al., 2004; Clift, 2006; Métivier & Gaudemer, 1999). Since ~9 Ma, both sedimentation rate models exhibit a similar stepwise increase in sediment accumulation rate (Figures 11a), although they show very distinct Quaternary mean values, with $\sim 0.05 \times 10^{12}$ kg yr^{-1} for Clift et al. (2004), who included the Pearl River mouth/South China marginal basins and Yangtze/East China marginal basins, to $\sim 0.6 \times 10^{12}$ kg yr^{-1} for Métivier et al. (1999), who included the Pearl River mouth, East China Sea, Yellow Sea, Bohai, and Okinawa basins. The large-scale capture of sediment onshore for the Yangtze system or the distinct glacial-interglacial change in erosion flux (Clift et al., 2006) may account for this inconsistency. The stepwise increase in sediment accumulation rate in East Asia marginal sea is also consistent with the average Asian mountain erosion rate that was analyzed by the low-temperature thermochronometry since ~8 Ma (Figures 11b; data from Herman et al., 2013), thus confirming the validity of relative change in sedimentation rate of East Asia marginal sea. However, the low-temperature thermochronometry data are mainly from bedrocks around the TP and its margins, therefore a mean of mountain

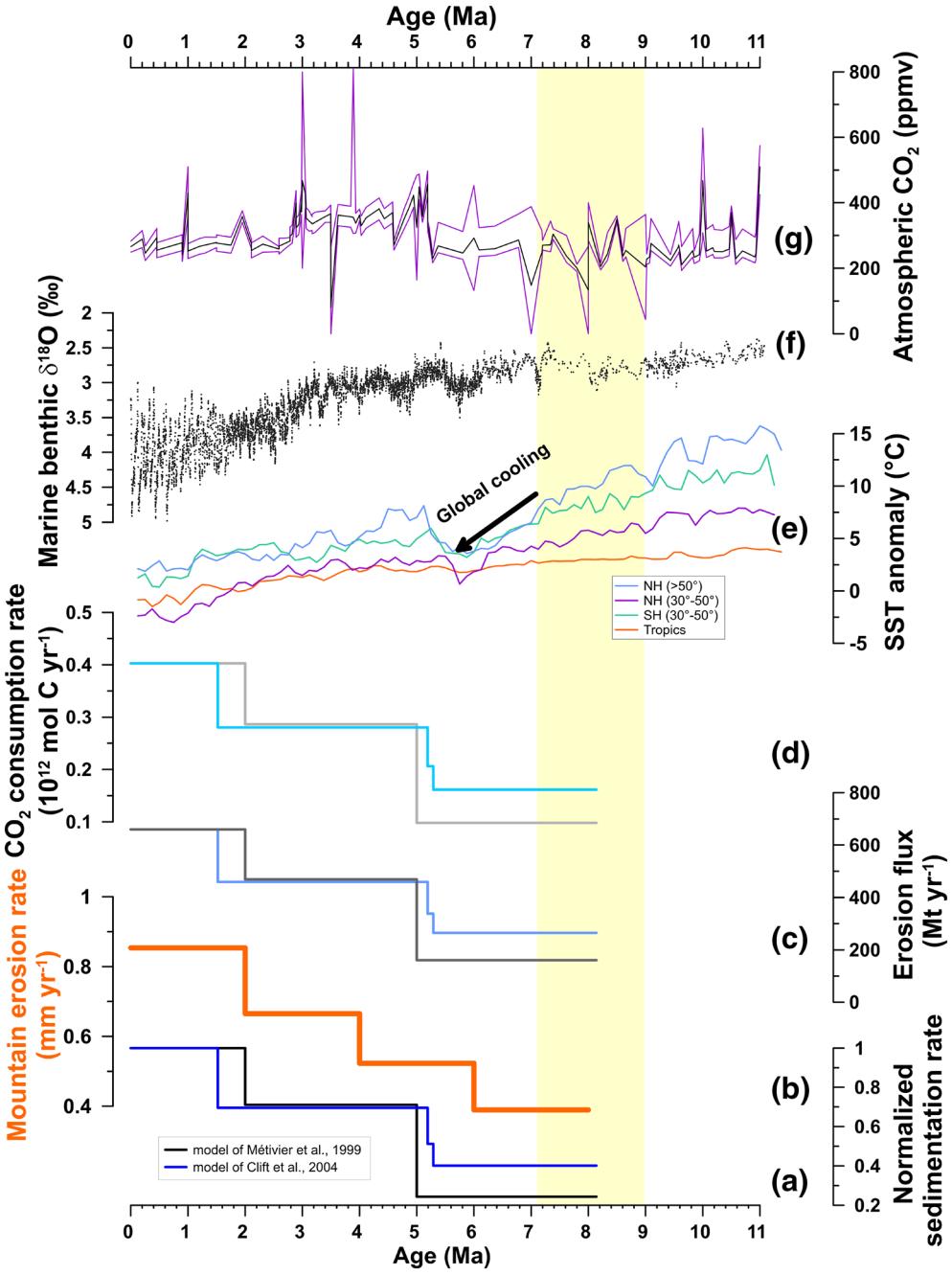

Figure 11. Estimated CO_2 consumption flux by silicate weathering in southern East China since ~8 Ma. (a) The relative change in sedimentation rate in East China normalized by mean values in the Quaternary. The black and blue lines in (a) are based on the East China Platform data set (Métivier et al., 1999) and integrative flux of the Pearl River and East China Sea basins (Clift et al., 2004), respectively. (b) Mountain erosion rate at Asia since ~8 Ma using low-temperature thermochronometry (data are from Herman et al., 2013; the curve shows arithmetic means of 8–6 Ma, 6–4 Ma, 4–2 Ma, and 2–0 Ma time periods, from 60 to 140°N and 20 to 45°E). (c) The erosion flux of the southern East China monsoon region, which is reconstructed by our estimated modern physical erosion flux of ~0.66×10^{12} kg·yr^{-1} for the southern East Asian monsoon region by multiplying the relative variation of the sedimentation rate in (a). (d) The estimated CO_2 consumption flux by silicate weathering (e) and its comparison with (f) the stacked SST anomalies for the Northern Hemisphere (NH), Southern Hemisphere (SH) and tropics (Herbert et al., 2016), (g) marine benthic oxygen isotope values (Zachos et al., 2001), and (g) atmospheric CO_2 concentrations (Beerling & Royer, 2011). Purple lines in (g) mark the lower and upper limits of the reconstructed CO_2 concentration by various proxies.

erosion rate at ~8–6 Ma (~0.4 mm yr^{-1}) (Figures 11b) cannot be directly used to estimate the erosion rate over the broad southern East China.

There are large floodplains in East Asia, in which the floodplain area of 541.9×10^3 km^2 for the Yangtze River is comparable to the large Ganga & Brahmaputra systems with a floodplain area of 716.9×10^3 km^2 (Wittman et al., 2020). Here, the equilibrium time of a sediment-routing system is used to characterize the time that it takes for this system to respond to a perturbation and then return to a steady state (Beaumont et al., 2000). The maximum equilibrium time for erosional and depositional processes in most sedimentary systems is commonly ~10^6 years (e.g., Romans et al., 2016). Because of the sufficient buffering capacity of extensive floodplains, the huge floodplains in East China will exhibit a longer equilibrium time at 10^5–10^6 years compared with the climatic oscillations at 10^4 years (e.g., Castelltort & Van Den Driessche, 2003; Covault et al., 2013; Métivier & Gaudemer, 1999). Our estimated present-day average sediment discharge is thus considered to have remained constant throughout the Quaternary for East China. Based on the relative changes in sedimentation rate in both budget models for the East Asian monsoon region (Figures 11a), the sediment accumulation rate since ~9 Ma for monsoon-influenced southern East China could be constructed based on the relative variations multiplied by our present estimated erosion flux of ~0.66×10^{12} kg·yr^{-1} (Figures 11c). Using the sedimentation budget model of Clift et al. (2004), the upper limit of the sedimentation rate estimate at ~8 Ma is 0.26×10^{12} kg yr^{-1} (Figures 11c), which is approximately 40% of the present erosion flux in modern southern East China.

Overall, a Δ_{sil} value of 0.61 mol C kg^{-1} for upper crust weathering over southern East China yields a CO_2 consumption flux for southern East China ranging from ~1.0×10^{11} mol C yr^{-1} (using the model of Métivier et al., 1999) to ~1.6×10^{11} mol C yr^{-1} (using the model of Clift et al., 2004) (Figures 11d) at ~8 Ma. The upper limit of the estimated CO_2 consumption flux for the entire East Asia monsoon region (including the CLP and southern East China) is thus ~1.8×10^{11} mol C yr^{-1}, accounting for 2% of the current continental silicate weathering sink (Figure 5; Gaillardet et al., 1999; Moon et al., 2014).

5.5. Implications

The estimated CO_2 consumption flux caused by enhanced silicate weathering in the East Asian monsoon region at ~8 Ma ranges from 0.18×10^{11} mol C yr^{-1} to ~1.8×10^{11} mol C yr^{-1}, which corresponds to 0.2%–2% of the current continental silicate weathering sink (Figure 5; Gaillardet et al., 1999; Moon et al., 2014). The carbon cycle should remain in a close balance (Berner & Caldeira, 1997). A modeling study further suggests that only a sustained 0.25%–0.5% increase in the silicate weathering rate globally with the varying strength of silicate weathering feedback is necessary to explain the long-term decline in the atmospheric CO_2 content over the Cenozoic (Caves et al., 2016; Caves Rugenstein et al., 2019). Our study thus suggests that the CO_2 sink arising from enhanced silicate weathering over the East Asia monsoon-influenced region likely has a significant role in the global carbon cycle because this climate-induced carbon sink represents an additional flux that can be incorporated into the existing global carbon budget since ~8 Ma. This emerging atmospheric CO_2 consumption mechanism differs from the long-existing mechanism, in which high erosion rates in tectonically active southern TP regions produce overall high silicate weathering fluxes and organic carbon burial rates (e.g., France-Lanord & Derry, 1997; Raymo et al., 1988). Compared with the southern TP region, the majority of the East Asian monsoon-influenced region was generally topographically low and tectonically less active under a crustal extension setting caused by the westward subduction of the Pacific Plate beneath the eastern edge of the Eurasian continent since the Mesozoic (L. G. Fan et al., 2019; Y. Zheng et al., 2013). This region could thus be reasonably regarded as being within a uniformly stable and low-erosion regime. In this regard, the increase in silicate weathering in East Asian monsoon regions could have acted as a potential geological sink for atmospheric CO_2 because the increase in the SWI caused by strong monsoon precipitation likely induced an increase in the silicate weathering flux.

Such enhanced weathering of the upper continental crust by the East Asian monsoon likely caused a rapid reduction in atmospheric CO_2 and a series of related feedback effects, e.g., an increase in continental weatherability that is regarded as a primary control of Neogene cooling (Caves Rugenstein et al., 2019) by involving a large area of less-altered eolian and fluvial deposits in the CLP. The maximum period of late Miocene global cooling, as evidenced by a remarkable decline in global sea surface temperature at ~7–5.4 Ma

(Figures 4d and 11e), supports a significant decline in the atmospheric CO_2 level (Herbert et al., 2016), which is difficult to discern in most existing pCO_2 reconstructions due to their significant uncertainties (Figures 11g, Beerling & Royer, 2011). Our study thus illustrated a new atmospheric CO_2 consumption mechanism (Figure 5), providing evidence that the CO_2 sink at ~9–7 Ma related to the intensification of the East Asian monsoon likely contributed to a lowering of atmospheric CO_2, which led to the maximum global cooling (Herbert et al., 2016) and development of the Northern Hemisphere ice sheet (Larsen et al., 1994) since ~7 Ma (Figure 5). The uplift of the TP has promoted CO_2 consumption not only through a strong erosion-driven generally low SWI but also through high silicate weathering flux in the tectonically active plateau region, as suggested by many previous studies (e.g., France-Lanord & Derry, 1997; Raymo & Ruddiman et al., 1992), as well as through intensifying the monsoon precipitation-driven enhanced intensity and flux of silicate weathering over the East Asian monsoon region, as shown by our study.

6. Conclusions

The chemical weathering processes on the northeastern TP and the adjacent western CLP region have exhibited a significant increase in the SWI at ~9–7 Ma. Based on the Na/Al-clay mineral assemblage correction, our study presents the first quantitative estimate of the maximum CO_2 consumption flux by enhanced silicate weathering over the East Asian monsoon-influenced region at ~8 Ma. The estimated flux of $\sim 0.18 \times 10^{11}$ mol C yr^{-1} for the lower limit of the CLP region and $\sim 1.6 \times 10^{11}$ mol C yr^{-1} for the upper limit for southern East China collectively yield a total CO_2 consumption flux in the entire East Asian monsoon region ranging from $\sim 0.18 \times 10^{11}$ mol C yr^{-1} to $\sim 1.8 \times 10^{11}$ mol C yr^{-1}, which accounts for 0.2%–2% of the modern continental silicate weathering flux. Our study suggests that the uplift-driven reorganization of the climatic pattern in tectonically less active East Asia might have played a significant role in the lowering of atmospheric CO_2, late Miocene global cooling and development of the Northern Hemisphere ice sheet starting at ~7 Ma. Given the considerable uncertainties in climatic reconstructions and sediment budgets, accurately estimating the flux of the climate-induced carbon sink and assessing its significance to the global carbon cycle need to be further verified using more precise geological archives.

Data Availability Statement

All data are available in the supporting information and are hosted in the figshare repository-DOI:https://doi.org/10.6084/m9.figshare.12477947

Acknowledgments
This study was co-supported by the Strategic Priority Research Program of the Chinese Academy of Sciences (Grant No. XDA20070201), the Second Tibetan Plateau Scientific Expedition and Research (STEP) program (Grant No. 2019QZKK0707), the National Natural Science Foundation of China (Grant Nos., 41771236 and 41620104002), and the Youth Innovation Promotion Association (2018095) of the Chinese Academy of Sciences. We are grateful to Song Yang for the meteorological data acquisition, Debo Zhao for the figure illustrations, and Zhangdong Jin, Jinbo Zan and Peter Clift for the helpful discussions. The thorough and helpful comments from Daniel Ibarra and the other anonymous reviewer are greatly appreciated. The authors declare no competing financial interests.

References

An, Z., Kutzbach, J. E., Prell, W. L., & Porter, S. C. (2001). Evolution of Asian monsoons and phased uplift of the Himalaya-Tibetan plateau since late Miocene times. *Nature*, *41*, 62–66. http://doi.org/10.1038/35075035

Anagnostou, E., John, E. H., Babila, T. L., Sexton, P. F., Ridgwell, A., Lunt, D. J., et al. (2020). Proxy evidence for state-dependence of climate sensitivity in the Eocene greenhouse. *Nature Communications*, *11*(1), 1–9. https://doi.org/10.1038/s41467-020-17887-x

Anagnostou, E., John, E. H., Edgar, K. M., Foster, G. L., Ridgwell, A., Inglis, G. N., et al. (2016). Changing atmospheric CO_2 concentration was the primary driver of early Cenozoic climate. *Nature*, *533*(7603), 380–384. https://doi.org/10.1038/nature17423

Ao, H., Roberts, A. P., Dekkers, M. J., Liu, X., Rohling, E. J., Shi, Z., et al. (2016). Late Miocene-Pliocene Asian monsoon intensification linked to Antarctic ice-sheet growth. *Earth and Planetary Science Letters*, *444*, 75–87. http://dx.doi.org/10.1016/j.epsl.2016.03.028

Barnhisel, R. I., & Bertsch, P. M. (1989). Chlorites and hydroxy-interlayered vermiculite and smectite. In J. B. Dixon, & S. B. Weed (Eds.), *Minerals in soil environments* (pp. 729–788). Soil Madison: Science Society of America. http://dx.doi.org/10.2136/sssabookser1.2ed.c15

Beaumont, C., Kooi, H., & Willett, S. (2000). Coupled tectonic-surface process models with applications to rifted margins and collisional orogens. In M. A. Summerfield (Ed.), *Geomorphology and global tectonics* (pp. 29–55). Chichester: Wiley.

Beerling, D. J., & Royer, D. L. (2011). Convergent Cenozoic CO2 history. *Nature Geoscience*, *4*, 418–420. http://dx.doi.org/10.1038/ngeo1186

Berner, R. A., & Caldeira, K. (1997). The need for mass balance and feedback in the geochemical carbon cycle. *Geology*, *25*, 955. http://dx.doi.org/10.1130/0091-7613(1997)025<0955:TNFMBA>2.3.CO;2

Bird, A., Millar, I., Rodenburg, T., Stevens, T., Rittner, M., Vermeesch, P., et al. (2020). A constant Chinese Loess Plateau dust source since the late Miocene. *Quaternary Science Reviews*, *227*, 106042. https://doi.org/10.1016/j.quascirev.2019.106042

Bolton, C. T., & Stoll, H. M. (2013). Late Miocene threshold response of marine algae to carbon dioxide limitation. *Nature*, *500*, 558–562. http://dx.doi.org/10.1038/nature12448

Castelltort, S., & Van Den Driessche, J. (2003). How plausible are high-frequency sediment supply-driven cycles in the stratigraphic record? *Sedimentary Geology*, *157*, 3–13. https://doi.org/10.1016/S0037-0738(03)00066-6

Caves Rugenstein, J. K., Ibarra, D. E., & von Blanckenburg, F. (2019). Neogene cooling driven by land surface reactivity rather than increased weathering fluxes. *Nature*, *571*(7763), 99–102. http://dx.doi.org/10.1038/s41586-019-1332-y

Caves, J. K., Jost, A. B., Lau, K. V., & Maher, K. (2016). Cenozoic carbon cycle imbalances and a variable silicate weathering feedback. *Earth and Planetary Science Letters*, *450*, 152–163. http://dx.doi.org/10.1016/j.epsl.2016.06.035

Cerling, T. E., Harris, J. M., MacFadden, B. J., Leakey, M. G., Quade, J., Eisenmann, V., et al. (1997). Global vegetation change through the Miocene/Pliocene boundary. *Nature*, *389*, 153–158. https://doi.org/10.1038/s41586-019-1332-y

Chamley, H. (1989). *Clay sedimentology*. Berlin: Springer-Verlag. http://dx.doi.org/10.1007/978-3-642-85916-8

Chappell, J., Zheng, H., & Fifield, K. (2006). Yangtze River sediments and erosion rates from source to sink traced with cosmogenic ^{10}Be: Sediments from major rivers. *Palaeogeography, Palaeoclimatology, Palaeoecology*, *241*, 79–94. https://doi.org/10.1016/j.palaeo.2006.06.010

Chen, Z., & Li, G. (2013). Evolving sources of eolian detritus on the Chinese Loess Plateau since early Miocene: Tectonic and climatic controls. *Earth and Planetary Science Letters*, *371*, 220–225. https://doi.org/10.1016/j.epsl.2013.03.044

Chen, F., Yu, Z., Yang, M., Ito, E., Wang, S., Madsen, D. B., et al. (2008). Holocene moisture evolution in arid central Asia and its out-of-phase relationship with Asian monsoon history. *Quaternary Science Reviews*, *27*, 351–364. https://doi.org/10.1016/j.quascirev.2007.10.017

Cleveland, W. S. (1979). Robust locally weighted regression and smoothing scatterplots. *Journal of the American Statistical Association*, *74*, 829–836. https://doi.org/10.1080/01621459.1979.10481038

Clift, P. D. (2006). Controls on the erosion of Cenozoic Asia and the flux of clastic sediment to the ocean. *Earth and Planetary Science Letters*, *241*, 571–580. https://doi.org/10.1016/j.epsl.2005.11.028

Clift, P. D., Hodges, K. V., Heslop, D., Hannigan, R., Van Long, H., & Calves, G. (2008). Correlation of Himalayan exhumation rates and Asian monsoon intensity. *Nature Geoscience*, *1*, 875–880. http://dx.doi.org/10.1038/ngeo351

Clift, P. D., Layne, G. D., & Blusztajn, J. (2004). Marine sedimentary evidence for monsoon strengthening, Tibetan uplift and drainage evolution in East Asia. Continent–ocean interactions within East Asian marginal seas. *Geophysical Monograph Series*, *149*, 255–282. https://doi.org/10.1029/149GM14

Clift, P. D., Wan, S., & Blusztajn, J. (2014). Reconstructing chemical weathering, physical erosion and monsoon intensity since 25 Ma in the northern south China sea: A review of competing proxies. *Earth-Science Reviews*, *130*, 86–102. https://doi.org/10.1016/j.earscirev.2014.01.002

CNEMC (China National Environmental Monitoring Centre). (1990). *Background values of elements in soils of China*. Beijing: China Environmental Science Press. https://doi.org/10.1007/BF00282934

Covault, J. A., Craddock, W. H., Romans, B. W., Fildani, A., & Gosai, M. (2013). Spatial and temporal variations in landscape evolution: Historic and longer-term sediment flux through global catchments. *The Journal of Geology*, *121*, 35–56. https://dx.doi.org/10.1086/668680

Ding, Z. L., Sun, J. M., Yang, S. L., & Liu, T. S. (2001). Geochemistry of the Pliocene red clay formation in the Chinese Loess Plateau and implications for its origin, source provenance and paleoclimate change. *Geochimica et Cosmochimica Acta*, *65*, 901–913. http://dx.doi.org/10.1016/S0016-7037(00)00571-8

Fang, X., Galy, A., Yang, Y., Zhang, W., Ye, C., & Song, C. (2019). Paleogene global cooling–induced temperature feedback on chemical weathering, as recorded in the northern Tibetan Plateau. *Geology*, *47*, 992–996. https://doi.org/10.1130/G46422.1

Fang, X., Wang, J., Zhang, W., Zan, J., Song, C., Yan, M., et al. (2016). Tectonosedimentary evolution model of an intracontinental flexural (foreland) basin for paleoclimatic research. *Global and Planetary Change*, *145*, 78–97. https://doi.org/10.1016/j.gloplacha.2016.08.015

Fan, L. G., Meng, Q. R., Wu, G. L., Wei, H. H., Du, Z. M., & Wang, E. (2019). Paleogene crustal extension in the eastern segment of the NE Tibetan plateau. *Earth and Planetary Science Letters*, *514*, 62–74. https://doi.org/10.1016/j.epsl.2019.02.036

Fan, M., Song, C., Dettman, D. L., Fang, X., & Xu, X. (2006). Intensification of the Asian winter monsoon after 7.4 Ma: Grain-size evidence from the Linxia basin, northeastern Tibetan plateau, 13.1 Ma to 4.3 Ma. *Earth and Planetary Science Letters*, *248*(1–2), 186–197. https://doi.org/10.1016/j.epsl.2006.05.025

Farnsworth, A., Lunt, D. J., O'Brien, C. L., Foster, G. L., Inglis, G. N., Markwick, P., et al. (2019). Climate sensitivity on geological timescales controlled by nonlinear feedbacks and ocean circulation. *Geophysical Research Letters*, *46*, 9880–9889. https://doi.org/10.1029/2019GL083574

France-Lanord, C., & Derry, L. A. (1997). Organic carbon burial forcing of the carbon cycle from Himalayan erosion. *Nature*, *390*, 65–67. https://doi.org/10.1038/36324

Fu, W., Li, X., Feng, Y., Feng, M., Peng, Z., Yu, H., et al. (2019). Chemical weathering of S-type granite and formation of Rare Earth Element (REE)-rich regolith in South China: Critical control of lithology. *Chemical Geology*, *520*, 33–51. http://dx.doi.org/10.1016/j.chemgeo.2019.05.006

Gaillardet, J., Dupré, B., Louvat, P., & Allègre, C. J. (1999). Global silicate weathering and CO_2 consumption rates deduced from the chemistry of large rivers. *Chemical Geology*, *159*, 3–30. https://doi.org/10.1016/S0009-2541(99)00031-5

Gao, S., Luo, T. C., Zhang, B. R., Zhang, H. F., Han, Y. W., Zhao, Z. D., et al. (1998). Chemical composition of the continental crust as revealed by studies in east China. *Geochimica et Cosmochimica Acta*, *62*, 1959–1975. https://doi.org/10.1016/S0016-7037(98)00121-5

Gao, Y., Wang, C., Liu, Z., Du, X., & Ibarra, D. E. (2015). Diagenetic and paleoenvironmental controls on late Cretaceous clay minerals in the Songliao basin, northeast China. *Clays and Clay Minerals*, *63*, 469–484. https://doi.org/10.1346/CCMN.2015.0630605

Guo, Z. T., Ruddiman, W. F., Hao, Q. Z., Wu, H. B., Qiao, Y. S., Zhu, R. X., et al. (2002). Onset of Asian desertification by 22 Myr ago inferred from loess deposits in China. *Nature*, *416*(6877), 159–163. https://doi.org/10.1038/416159a

Guo, Z. T., Peng, S. Z., Hao, Q. Z., Biscaye, P. E., & Liu, T. S. (2001). Origin of the Miocene-Pliocene red-earth formation at Xifeng in northern China and implications for paleoenvironments. *Palaeogeography, Palaeoclimatology, Palaeoecology*, *170*, 11–26. http://dx.doi.org/10.1016/s0031-0182(01)00235-8

Hansen, J., Sato, M., Russell, G., & Kharecha, P. (2013). Climate sensitivity, sea level and atmospheric carbon dioxide. *Philosophical Transactions of the Royal Society A*, *371*, 20120294. https://doi.org/10.1098/rsta.2012.0294

Herbert, T. D., Lawrence, K. T., Tzanova, A., Peterson, L. C., Caballero-Gill, R., & Kelly, C. S. (2016). Late Miocene global cooling and the rise of modern ecosystems. *Nature Geoscience*, *9*, 843–847. http://dx.doi.org/10.1038/ngeo2813

Herman, F., Seward, D., Valla, P. G., Carter, A., Kohn, B., Willett, S. D., & Ehlers, T. A. (2013). Worldwide acceleration of mountain erosion under a cooling climate. *Nature*, *504*(7480), 423–426. https://doi.org/10.1038/nature12877

Hong, H., Wang, C., Zeng, K., Gu, Y., Wu, Y., Yin, K., et al. (2013). Geochemical constraints on provenance of the mid-Pleistocene red earth sediments in subtropical China. *Sedimentary Geology*, *290*, 97–108. https://doi.org/10.1016/j.sedgeo.2013.03.008

Larsen, H. C., Saunders, A. D., Clift, P. D., Beget, J., Wei, W., & Spezzaferri, S. (1994). ODP leg 152 Scientific Party. Seven million years of glaciation in Greenland. *Science*, *264*, 952–955. http://dx.doi.org/10.1126/science.264.5161.952

Lease, R. O., Burbank, D. W., Gehrels, G. E., Wang, Z., & Yuan, D. (2007). Signatures of mountain building: Detrital zircon U/Pb ages from northeastern Tibet. *Geology*, *35*, 239–242. http://dx.doi.org/10.1130/G23057A.1

Lenard, S. J., Lavé, J., France-Lanord, C., Aumaître, G., Bourlès, D. L., & Keddadouche, K. (2020). Steady erosion rates in the Himalayas through late Cenozoic climatic changes. *Nature Geoscience*, *13*, 448–452. https://doi.org/10.1038/s41561-020-0585-2

Liang, M., Guo, Z., Kahmann, A. J., & Oldfield, F. (2009). Geochemical characteristics of the Miocene eolian deposits in China: Their provenance and climate implications. *Geochemistry, Geophysics, Geosystems*, *10*, Q04004. https://doi.org/10.1029/2008GC002331
Licht, A., Pullen, A., Kapp, P., Abell, J., & Giesler, N. (2016). Eolian cannibalism: Reworked loess and fluvial sediment as the main sources of the Chinese Loess Plateau. *The Geological Society of America Bulletin*, *128*(5–6), 944–956. https://doi.org/10.1130/B31375.1
Li, J., Fang, X., Song, C., Pan, B., Ma, Y., & Yan, M. (2014). Late Miocene-Quaternary rapid stepwise uplift of the NE Tibetan Plateau and its effects on climatic and environmental changes. *Quaternary Research*, *81*, 400–423. https://doi.org/10.1016/j.yqres.2014.01.002
Liu, T. S. (1985). *Loess and the environment*. Beijing: China Ocean Press.
Liu, X. D., & Dong, B. W. (2013). Influence of the Tibetan Plateau uplift on the Asian monsoon-arid environment evolution. *Chinese Science Bulletin*, *58*, 4277–4291. https://doi.org/10.1007/s11434-013-5987-8
Liu, S., Li, J., Stockli, D. F., Song, C., Guo, B., Stockli, L. D., et al. (2019). Reappraisal of Miocene eolian deposition in Tianshui Basin, China, based on an investigation of stratigraphy and provenance. *The Geological Society of America Bulletin*, *131*(7–8), 1312–1332. https://doi.org/10.1130/B32056.1
Liu, J. P., Xu, K. H., Li, A. E. A., Milliman, J. D., Velozzi, D. M., Xiao, S. B., et al. (2007). Flux and fate of Yangtze River sediment delivered to the east China sea. *Geomorphology*, *85*(3–4), 208–224. https://doi.org/10.1016/j.geomorph.2006.03.023
Li, Z., Yan, G., Wang, Y., Pan, Y., Li, J., Chen, A., et al. (2015). Can monsoon moisture arrive in the Qilian Mountains in summer? *Quaternary International*, *358*, 113–125. http://dx.doi.org/10.1016/j.quaint.2014.08.046
Lu, H., Liu, R., Cheng, L., Feng, H., Zhang, H., Wang, Y., et al. (2020). Phased evolution and variation of the South Asian monsoon, and resulting weathering and surface erosion in the Himalaya–Karakoram Mountains, since late Pliocene time using data from Arabian Sea core. *Geological Magazine*, 1–15. https://doi.org/10.1017/S0016756820000291
Lupker, M., France-Lanord, C., Galy, V., Lavé, J., Gaillardet, J., Gajurel, A. P., et al. (2012). Predominant floodplain over mountain weathering of Himalayan sediments (Ganga basin). *Geochimica et Cosmochimica Acta*, *84*, 410–432. http://dx.doi.org/10.1016/j.gca.2012.02.001
Macdonald, F. A., Swanson-Hysell, N. L., Park, Y., Lisiecki, L., & Jagoutz, O. (2019). Arc-continent collisions in the tropics set Earth's climate state. *Science*, *364*(6436), 181–184. http://dx.doi.org/10.1126/science.aav5300
Ma, Y., Fang, X., Li, J., Wu, F., & Zhang, J. (2005). The vegetation and climate change during Neocene and Early Quaternary in Jiuxi Basin, China. *Science in China - Series D: Earth Sciences*, *48*(5), 676. http://dx.doi.org/10.1360/03yd0110
Métivier, F., & Gaudemer, Y. (1999). Stability of output fluxes of large rivers in south and east Asia during the last 2 million years: Implications on floodplain processes. *Basin Research*, *11*, 293–303. https://doi.org/10.1046/j.1365-2117.1999.00101.x
Métivier, F., Gaudemer, Y., Tapponnier, P., & Klein, M. (1999). Mass accumulation rates in Asia during the Cenozoic. *Geophysical Journal of the Royal Astronomical Society*, *137*(2), 280–318. https://doi.org/10.1046/j.1365-246X.1999.00802.x
Miao, Y., Fang, X., Herrmann, M., Wu, F., Zhang, Y., & Liu, D. (2011). Miocene pollen record of KC-1 core in the Qaidam Basin, NE Tibetan Plateau and implications for evolution of the East Asian monsoon. *Palaeogeography, Palaeoclimatology, Palaeoecology*, *299*(1–2), 30–38. http://dx.doi.org/10.1016/j.palaeo.2010.10.026
Milliman, J. D., & Meade, R. H. (1983). World-wide delivery of river sediment to the oceans. *The Journal of Geology*, *91*(1), 1–21. https://doi.org/10.1086/628741
Milliman, J. D., & Syvitski, P. M. (1992). Geomorphic/tectonic control of sediment discharge to the ocean: The importance of small mountainous rivers. *The Journal of Geology*, *100*, 525–544. http://dx.doi.org/10.2307/30068527
Milliman, J. D., Yun-Shan, Q., Mei-e, R., & Saito, Y. (1987). Man's influence on the erosion and transport of sediment by Asian rivers: The Yellow River (Huanghe) example. *The Journal of Geology*, *95*(6), 751–762. https://doi.org/10.1086/629175
Molnar, P. (2005). The growth of the Tibetan plateau and Mio-pliocene evolution of East Asian climate. *Palaeontologia Electronica*, *8*(1), 1–23. http://dx.doi.org/10.1016/j.palaeo.2009.11.002
Moon, S., Chamberlain, C. P., & Hilley, G. E. (2014). New estimates of silicate weathering rates and their uncertainties in global rivers. *Geochimica et Cosmochimica Acta*, *134*, 257–274. http://dx.doi.org/10.1016/j.gca.2014.02.033
Moore, D. M., & Reynolds, R. C. (1997). *X-ray diffraction and the identification and analysis of clay minerals* (2nd ed.). New York: Oxford University Press. http://dx.doi.org/10.1180/claymin-1999-s2
Muller, R. D., Sdrolias, M., Gaina, C., Steinberger, B., & Heine, C. (2008). Long-term sea-level fluctuations driven by ocean basin dynamics. *Science*, *319*, 1357–1362. http://dx.doi.org/10.1126/science.1151540
Nesbitt, H. W., Fedo, C. M., & Young, G. M. (1997). Quartz and feldspar stability, steady and non-steady-state weathering, and petrogenesis of siliciclastic sands and muds. *The Journal of Geology*, *105*, 173–192. http://dx.doi.org/10.1086/515908
Nesbitt, H. W., & Young, G. M. (1982). Early Proterozoic climates and plate motions inferred from major element chemistry of lutites. *Nature*, *299*, 715–717. https://doi.org/10.1038/299715a0
Nesbitt, H. W., Young, G. M., McLennan, S. M., & Keays, R. R. (1996). Effects of chemical weathering and sorting on the petrogenesis of siliciclastic sediments, with implications for provenance studies. *The Journal of Geology*, *104*, 525–542. https://doi.org/10.1086/629850
Nie, J., Garzione, C., Su, Q., Liu, Q., & Zhang, R. (2017). Dominant 100,000-year precipitation cyclicity in a late Miocene lake from northeast Tibet. *Science Advances*, *3*(3), e1600762. http://dx.doi.org/10.1126/sciadv.1600762
Nie, J., Peng, W., Möller, A., Song, Y., Stockli, D. F., Stevens, T., et al. (2014). Provenance of the upper Miocene-Pliocene Red Clay deposits of the Chinese loess plateau. *Earth and Planetary Science Letters*, *407*, 35–47. http://dx.doi.org/10.1016/j.epsl.2014.09.026
Nie, J., Stevens, T., Rittner, M., Stockli, D., Garzanti, E., Limonta, M., et al. (2015). Loess plateau storage of northeastern Tibetan plateau-derived Yellow River sediment. *Nature Communications*, *6*(1), 8511. http://dx.doi.org/1-10.0.1038/ncomms9511
Ogg, J. G. (2012). Geomagnetic polarity time scale. In F. M. Gradstein, J. G. Ogg, M. D. Schmitz, & G. M. Ogg (Eds.), *The geologic time scale 2012* (pp. 85–114). Hoboken, NJ: Elsevier.
Park, Y., Maffre, P., Goddéris, Y., Macdonald, F. A., Anttila, E. S., & Swanson-Hysell, N. L. (2020). Emergence of the southeast Asian islands as a driver for Neogene cooling. *Proceedings of the National Academy of Sciences USA*, *117*(41), 25319–25326. http://dx.doi.org/10.1073/pnas.2011033117
Qiang, X. K., Li, Z. X., Powell, C. M., & Zheng, H. B. (2001). Magnetostratigraphic record of the late Miocene onset of the East Asian monsoon and Pliocene uplift of northern Tibet. *Earth and Planetary Science Letters*, *187*, 83–93. http://dx.doi.org/10.1016/S0012-821X(01)00281-3
Rasmussen, C., Brantley, S., Blum, A., Dixon, J., & White, A. F. (2011). Strong climate and tectonic control on plagioclase weathering in granitic terrain. *Earth and Planetary Science Letters*, *30*, 521–530. http://dx.doi.org/10.1016/j.epsl.2010.11.037
Raymo, M. E., & Ruddiman, W. F. (1992). Tectonic forcing of late Cenozoic climate. *Nature*, *359*, 117–122. https://doi.org/10.1038/359117a0
Raymo, M. E., Ruddiman, W. F., & Froelich, P. N. (1988). Influence of late Cenozoic mountain building on ocean geochemical cycles. *Geology*, *16*(7), 649–653.
Rea, D. K., Snoeckx, H., & Joseph, L. H. (1998). Late Cenozoic Eolian deposition in the north pacific: Asian drying, Tibetan uplift, and cooling of the northern hemi-sphere. *Paleoceanography and Paleoceanography*, *13*, 215–224. https://doi.org/10.1029/98PA00123

Reynolds, R. C. (1980). Interstratified clay minerals. In G. W. Brindley, & G. Brown (Eds.), *Crystal structures of clay minerals and their X-ray identification* (pp. 249–303). London: Mineralogical Society. http://dx.doi.org/10.1180/mono-5.4

Rohling, E. J., Sluijs, A., Dijkstra, H. A., Köhler, P., van de Wal, R. S., von der Heydt, D. J., et al. (2012). Making sense of palaeoclimate sensitivity. *Nature*, *491*(7426), 683–691. https://doi.org/10.1038/nature11574

Romans, B. W., Castelltort, S., Covault, J. A., Fildani, A., & Walsh, J. P. (2016). Environmental signal propagation in sedimentary systems across timescales. *Earth-Science Reviews*, *153*, 7–29. http://dx.doi.org/10.1016/j.earscirev.2015.07.012

Ruan, X., Yang, Y., Galy, A., Fang, X., Jin, Z., Zhang, F., et al. (2019). Evidence for early (≥12.7 Ma) eolian dust impact on river chemistry in the northeastern Tibetan Plateau. *Earth and Planetary Science Letters*, *515*, 79–89 https://doi.org/10.1016/j.epsl.2019.03.022

Ruddiman, W. F., & Kutzbach, J. E. (1990). Late Cenozoic plateau uplift and climate change. *Transaction of the Royal Society of Edinburgh: Earth and Environmental Science*, *81*, 301–314. http://dx.doi.org/10.1017/S0263593300020812

Rudnick, R. L., & Gao, S. (2003). Composition of the continental crust. In H. D. Holland, & K. K. Turekian (Eds.), *The crust. Treatise on geochemistry* (pp. 1–64). Oxford: Elsevier https://doi.org/10.1016/B978-0-08-095975-7.00301-6

Ruxton, B. P. (1968). Measures of the degree of chemical weathering of rocks. *The Journal of Geology*, *76*, 518–527. http://dx.doi.org/10.2307/30066179

Saylor, J. E., Jordan, J. C., Sundell, K. E., Wang, X., Wang, S., & Deng, T. (2018). Topographic growth of the Jishi Shan and its impact on basin and hydrology evolution, NE Tibetan Plateau. *Basin Research*, *30*, 544–563. http://dx.doi.org/10.1111/bre.12264

Shen, X., Wan, S., France-Lanord, C., Clift, P. D., Tada, R., Révillon, S., et al. (2017). History of asian eolian input to the sea of Japan since 15 Ma: Links to Tibetan uplift or global cooling?. *Earth and Planetary Science Letters*, *474*, 296–308. http://dx.doi.org/10.1016/j.epsl.2017.06.053

Song, Y. G., Fang, X. M., Li, J. J., An, Z. S., & Miao, X. D. (2001). The late Cenozoic uplift of the Liupan Shan, China. *Science in China Series D: Earth Science*, *44*, 176–184. http://dx.doi.org/10.1007/BF02911985

Sun, Y., & An, Z. (2002). History and variability of Asian interior aridity recorded by Eolian flux in the Chinese loess plateau during the past 7 Ma. *Science in China Series D: Earth Science*, *45*, 420–429. http://dx.doi.org/10.1360/02yd9044

Sun, H., & Liu, X. (2018). Impacts of the uplift of four mountain ranges on the arid climate and dust cycle of inland Asia. *Palaeogeography, Palaeoclimatology, Palaeoecology*, *505*, 167–179. https://doi.org/10.1016/j.palaeo.2018.05.040

Sun, Y., Lu, H., & An, Z. (2006). Grain size of loess, palaeosol and Red Clay deposits on the Chinese Loess Plateau: Significance for understanding pedogenic alteration and palaeomonsoon evolution. *Palaeogeography, Palaeoclimatology, Palaeoecology*, *241*, 129–138. https://doi.org/10.1016/j.palaeo.2006.06.018

Sun, Y., Ma, L., Bloemendal, J., Clemens, S., Qiang, X., & An, Z. (2015). Miocene climate change on the Chinese Loess Plateau: Possible links to the growth of the northern Tibetan Plateau and global cooling. *Geochemistry, Geophysics, Geosystems*, *16*, 2097–2108. https://doi.org/10.1002/2015GC005750

Sun, Y., Tada, R., Chen, J., Liu, Q., Toyoda, S., Tani, A., et al. (2008). Tracing the provenance of fine-grained dust deposited on the central Chinese Loess Plateau. *Geophysical Research Letters*, *35*(1), L01804. http://dx.doi.org/10.1029/2007GL031672

Tada, R., Zheng, H., & Clift, P. D. (2016). Evolution and variability of the Asian monsoon and its potential linkage with uplift of the Himalaya and Tibetan Plateau. *Progress in Earth and Planetary Science*, *3*(1), 4. https://doi.org/10.1186/s40645-016-0080-y

Tang, H., Micheels, A., Eronen, J. T., Ahrens, B., & Fortelius, M. (2013). Asynchronous responses of East Asian and Indian summer monsoons to mountain uplift shown by regional climate modeling experiments. *Climate Dynamics*, *40*(5–6), 1531–1549. https://doi.org/10.1007/s00382-012-1603-x

Taylor, W. (2000). *Change-Point Analyzer 2.0 shareware program*. Libertyville, IL: Taylor Enterprises. http://www.variation.com/cpa

Taylor, S. R., & McLennan, S. M. (1985). *The continental crust: Its composition and evolution*. Oxford: Blackwell Scientific Publication. http://dx.doi.org/10.1016/0031-9201(86)90093-2

Van Hoang, L., Clift, P. D., Schwab, A. M., Huuse, M., Nguyen, D. A., & Zhen, S. (2010). Large-scale erosional response of SE Asia to monsoon evolution reconstructed from sedimentary records of the Song Hong-Yinggehai and Qiongdongnan basins, South China Sea. *Geological Society, London, Special Publications*, *342*(1), 219–244. https://doi.org/10.1144/SP342.13

Walling, D. E., & Webb, B. W. (1983). Pattern of sediment yield. In K. J. Gregory (Ed.), *Background to Palaeo-hydrology* (pp. 69–100). New York: Wiley. https://doi.org/10.1017/S0016756800030302

Wan, S., Clift, P. D., Li, A., Li, T., & Yin, X. (2010). Geochemical records in the south China sea: Implications for East Asian summer monsoon evolution over the last 20 Ma. *Geological Society, London, Special Publications*, *342*(1), 245–263. https://doi.org/10.1144/SP342.14

Wan, S., Clift, P. D., Li, A., Yu, Z., Li, T., & Hu, D. (2012). Tectonic and climatic controls on long-term silicate weathering in Asia since 5 Ma. *Geophysical Research Letters*, *39*(15), L15611. https://doi.org/10.1029/2012GL052377

Wan, S., Li, A., Clift, P. D., & Stuut, J.-B, W. (2007a). Development of the East Asian monsoon: Mineralogical and sedimentologic records in the northern south China sea since 20 Ma. *Palaeogeography, Palaeoclimatology, Palaeoecology*, *254*(3–4), 561–582. https://doi.org/10.1016/j.palaeo.2007.07.009

Wan, S., Li, A., Jan-Berend, W. S., & Xu, F. (2007b). Grain-size records at ODP site 1146 from the northern south China sea: Implications on the East Asian monsoon evolution since 20 Ma. *Science in China Series D: Earth Sciences*, *50*(10), 1536–1547. http://dx.doi.org/10.1007/s11430-007-0082-0

Wang, X., Carrapa, B., Sun, Y., Dettman, D. L., Chapman, J. B., Caves Rugenstein, J. K., et al. (2020). The role of the westerlies and orography in Asian hydroclimate since the late Oligocene. *Geology*, *48*(7), 728–732. http://dx.doi.org/10.1130/G47400.1

Wedepohl, H. (1995). The composition of the continental crust. *Geochimica et Cosmochimica Acta*, *59*, 1217–1239. https://doi.org/10.1016/0016-7037(95)00038-2

Winnick, M. J., & Maher, K. (2018). Relationships between CO_2, thermodynamic limits on silicate weathering, and the strength of the silicate weathering feedback. *Earth and Planetary Science Letters*, *485*, 111–120. http://dx.doi.org/10.1016/j.epsl.2018.01.005

Wittmann, H., Oelze, M., Gaillardet, J., Garzanti, E., & von Blanckenburg, F. (2020). A global rate of denudation from cosmogenic nuclides in the Earth's largest rivers. *Earth-Science Reviews*, *204*, 103147. http://dx.doi.org/10.1016/j.earscirev.2020.103147

Xiong, S., Ding, Z., Zhu, Y., Zhou, R., & Lu, H. (2010). A ~ 6 Ma chemical weathering history, the grain size dependence of chemical weathering intensity, and its implications for provenance change of the Chinese loess-red clay deposit. *Quaternary Science Reviews*, *29*, 1911–1922. http://dx.doi.org/10.1016/j.quascirev.2010.04.009

Xiong, Y., & Li, Q. (1990). *Soils of China*. Beijing: Science Press.

Yang, Y., Fang, X., Galy, A., Jin, Z., Wu, F., Yang, R., et al. (2016). Plateau uplift forcing climate change around 8.6 Ma on the northeastern Tibetan Plateau: Evidence from an integrated sedimentary Sr record. *Palaeogeography, Palaeoclimatology, Palaeoecology*, *461*, 418–431. http://dx.doi.org/10.1016/j.palaeo.2016.09.002

Yang, Y., Fang, X., Li, M., Galy, A., Koutsodendris, A., & Zhang, W. (2015). Paleoenvironmental implications of uranium concentrations in lacustrine calcareous clastic-evaporite deposits in the western Qaidam Basin. *Palaeogeography, Palaeoclimatology, Palaeoecology*, *417*, 422–431. https://doi.org/10.1016/j.palaeo.2014.10.002

Yang, Y., Galy, A., Fang, X., Yang, R., Zhang, W., & Zan, J. (2017). Eolian dust forcing of river chemistry on the northeastern Tibetan Plateau since 8 Ma. *Earth and Planetary Science Letters*, *464*, 200–210. https://doi.org/10.1016/j.epsl.2017.02.009

Yang, R., Yang, Y., Fang, X., Ruan, X., Galy, A., Ye, C., et al. (2019). Late Miocene intensified tectonic uplift and climatic aridification on the northeastern Tibetan plateau: Evidence from clay mineralogical and geochemical records in the Xining Basin. *Geochemistry, Geophysics, Geosystems*, *20*, 829–851. http://dx.doi.org/10.1029/2018GC007917

Zachos, J., Pagani, M., Sloan, L., Thomas, E., & Billups, K. (2001). Trends, rhythms, and aberrations in global climate 65 Ma to present. *Science*, *292*(5517), 686–693. http://dx.doi.org/10.1126/science.1059412

Zan, J., Fang, X., Yan, M., Zhang, W., & Zhang, Z. (2015). Magnetic variations in surface soils in the NE Tibetan Plateau indicating the climatic boundary between the Westerly and East Asian summer monsoon regimes in NW China. *Global and Planetary Change*, *130*, 1–6. http://doi.org/10.1016/j.gloplacha.2015.03.008

Zan, J., Fang, X., Zhang, W., Yan, M., & Zhang, D. (2018). A new record of late Pliocene-early Pleistocene Eeolian loess–red clay deposits from the western Chinese Loess Plateau and its palaeoenvironmental implications. *Quaternary Science Reviews*, *186*, 17–26. https://doi.org/10.1016/j.quascirev.2018.02.010

Zhai, Y., & Cai, T. (1984). The Tertiary system of Gansu province. *Gansu Geology* (pp. 1–40). China: People's Press of Gansu.

Zhang, R., Jiang, D., Liu, X., & Tian, Z. (2012). Modeling the climate effects of different subregional uplifts within the Himalaya-Tibetan Plateau on Asian summer monsoon evolution. *Chinese Science Bulletin*, *57*, 4617–4626. https://doi.org/10.1007/s11434-012-5284-y

Zhang, J. X., Lu, J., Xing, X. D., Shen, Z. J., Lü, H. Z., & Zhang, G. L. (2007). Element geochemistry of laterite in the Dongting Lake area, Hunan, China and its indicative significance. *Geological Bulletin of China*, *26*, 1435–1444.(in Chinese).

Zhang, R., Zhang, Z., & Jiang, D. (2018). Global cooling contributed to the Establishment of a modern-like East Asian monsoon climate by the early Miocene. *Geophysical Research Letters*, *45*(21), 11–941. https://doi.org/10.1029/2018GL079930

Zhao, D., Wan, S., Clift, P. D., Tada, R., Huang, J., Yin, X., et al. (2018). Provenance, sea-level and monsoon climate controls on silicate weathering of Yellow River sediment in the northern Okinawa Trough during late last glaciation. *Palaeogeography, Palaeoclimatology, Palaeoecology*, *490*, 227–239. http://dx.doi.org/10.1016/j.palaeo.2017.11.002

Zheng, Y., Xiao, W., & Zhao, G. (2013). Introduction to tectonics of China. *Gondwana Research*, *23*, 1189–1206. https://doi.org/10.1016/j.gr.2012.10.001

Zheng, D. W., Zhang, P. Z., Wan, J. L., Yuan, D. Y., Li, C. Y., Yin, G. M., et al. (2006). Rapid exhumation at ∼8 Ma on the Liupan Shan thrust fault from apatite fission-track thermochronology: Implications for growth of the northeastern Tibetan Plateau margin. *Earth and Planetary Science Letters*, *248*, 198–208. http://dx.doi.org/10.1016/j.epsl.2006.05.023

Zoura, D., Hill, D. J., Dolan, A. M., Hunter, S. J., Tang, Z., & Haywood, A. M. (2019). Atmospheric carbon dioxide, ice sheet and topographic constraints on palaeo moisture availability in Asia. *Earth and Planetary Science Letters*, *519*, 12–27. http://dx.doi.org/10.1016/j.epsl.2019.04.035